The PMIP3 Simulated Climate Changes over Arid Central Asia during the Mid-Holocene and Last Glacial Maximum

XU Hongna[1], WANG Tao[1, 2, 3, *], WANG Huijun[1, 2, 3, 4], MIAO Jiapeng[3, 5], CHEN Jianhui[6] and CHEN Shengqian[6]

[1] *Collaborative Innovation Center on Forecast and Evaluation of Meteorological Disasters, Nanjing University of Information Science and Technology, Nanjing, 210044, China*
[2] *Climate Change Research Center, Chinese Academy of Sciences, Beijing 100029, China*
[3] *Nansen-Zhu International Research Center, Institute of Atmospheric Physics, Chinese Academy of Sciences, Beijing 100029, China*
[4] *Key Laboratory of Meteorological Disaster, Nanjing University of Information Science and Technology, Nanjing, 210044, China*
[5] *University of Chinese Academy of Sciences, Beijing, China*
[6] *Key Laboratory of Western China's Environmental Systems, College of Earth and Environmental Sciences, Lanzhou University, Lanzhou 730000, China*

Abstract: In this study, the climate changes over arid central Asia (ACA) during the mid-Holocene (approximately 6,000 calendar years ago, MH) and the Last Glacial Maximum (approximately 21,000 calendar years ago, LGM) are investigated using multimodel simulations derived from the Paleoclimate Modelling Intercomparison Project Phase 3 (PMIP3). During the MH, the multimodel median (MMM) shows that in the core region of ACA, the regionally averaged annual surface air temperature (SAT) decreases by 0.13°C and annual precipitation decreases by 3.45%, compared with the preindustrial (PI) climate. The MMM of the SAT increases by 1.67/0.13°C in summer/autumn, whereas it decreases by 1.23/1.11°C in spring/winter. The amplitude of the seasonal cycles of the SAT increases over ACA due to different MH orbital parameters. For precipitation, the regionally averaged MMM decreases by 5.77%/5.69%/0.39%/5.24% in spring/summer/autumn/winter, respectively. Based on the analysis of the aridity index (AI), compared with the PI, a drier climate appears in southern Central Asia and western Xinjiang due to decreasing precipitation. During the LGM, the MMM shows that the regionally averaged SAT decreases by 5.04/4.36/4.70/5.12/5.88°C and precipitation decreases by 27.78%/28.16%/31.56%/27.74%/23.29% annually and in the spring, summer, autumn, and winter, respectively. Robust drying occurs throughout almost the whole core area. Decreasing precipitation plays a dominant role in shaping the drier conditions, whereas strong cooling plays a secondary but opposite role. In response to the LGM external forcings, over Central Asia and Xinjiang, the seasonal cycle of precipitation has a smaller amplitude compared with that under the PI climate. In the model-data comparison, the simulated MH moisture changes over ACA are to some extent consistent with the reconstructions, further confirming that drier conditions occurred during that period than during the PI.

Key words: PMIP3, climate changes, arid central Asia, mid-Holocene, Last Glacial Maximum

E–mail: wangtao@mail.iap.ac.cn

1 Introduction

The mid-latitude Asian climate can be roughly divided into two main patterns based on whether it is mainly dominated by westerlies or by monsoon circulation at a large scale (Chen et al., 2009a). The westerlies-dominated Asia is also referred to as arid central Asia (ACA), and geographically, its core zone is approximately equivalent to Central Asia and Xinjiang area in China (Fig.1, Huang et al., 2015; Chen et al., 2019). Located over the central Eurasia continent, with the blocking of the Tibet-Pamir Plateau and Tianshan Mountain, ACA mainly gains water vapor through the westerlies from the remote area of the North Atlantic and the Mediterranean Sea (Chen et al., 2013). In addition, the Xinjiang area is also affected by monsoons (Chen et al., 2015). Thus, the unique geographical location and topography shapes the temperate-warm temperate continental climate and heavy droughts of this area (Chen et al., 2013).

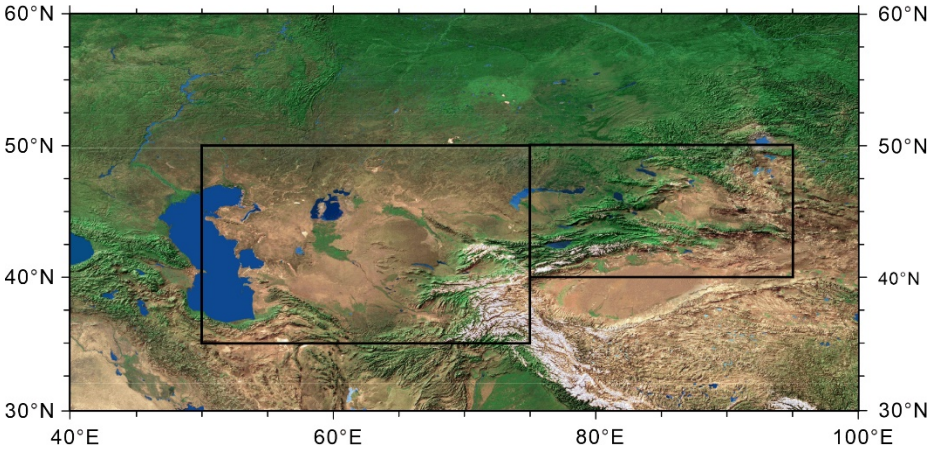

Fig. 1. Map shows the core zone of arid Central Asia, including Central Asia (35°–50°N, 50°–75°E, the left rectangle) and Xinjiang area in China (40°–50°N, 75°–95°E, the right rectangle).

Over ACA, the fragile ecosystem could be relatively sensitive to climate variabilities, especially precipitation (Huang et al., 2013). Based on previous studies (e.g., Yang et al., 2018; Guan et al., 2019), precipitation over Central Asia reaches its maximum in spring and winter, whereas precipitation over the Xinjiang area peaks in summer. The annual precipitation over most regions of ACA is less than 300 mm, even less than 50 mm over the desert regions (Yang et al., 2018). The annual and seasonal precipitation over Central Asia both showed an increasing trend in the period of 1930–2009 (Chen et al., 2011), and similar precipitation trend can be found over Xinjiang area since 1961 (Wang et al., 2017). At the same time, a strong warming trend (0.18°C/decade) has been observed over ACA, which was almost twice that over the Northern Hemisphere (NH) (Chen et al., 2009b). Additionally, because of global warming, the Xinjiang climate has changed from warm-dry to warm-wet since the mid-1980s (Shi et al., 2007; Jiang et al., 2009). However, some related processes and mechanisms are still unclear.

The mid-Holocene (approximately 6,000 calendar years ago, MH) is a well-known warm climate interval that occurred in the last ten thousand years. Due to the MH-altered orbital parameters, the NH received more insolation in summer, whereas less insolation in winter than at present (Berger, 1978). As a result, the seasonal cycle of the NH climate is strengthened. The reconstructed data suggest that the global annual temperature increased by ~0.7°C and that the extratropical NH temperature increased by ~1°C at approximately 8–6 ka with respect to that of the preindustrial (PI) level (Marcott et al., 2013). Over China, an increase of 1–4°C in annual surface temperature and an increase of 40%–100% in precipitation have been proposed by proxy data summarized in Wang et al (2010). For ACA and adjacent areas, some limited reconstruction suggests a wetter climate (Overeem et al., 2003; An et al., 2006; Chen et al., 2008; Yang and Zhu, 2018; Zhang et al., 2018a). Focusing on the MH, a large number of modeling studies have been carried out (e.g., Braconnot et al., 2007a, 2007b; Zhou and Zhao, 2009; Jiang et al., 2015a). The Paleoclimate Modelling Intercomparison Project (PMIP) considers the MH as one of the periods of concern (Joussaume and Taylor, 1995; Braconnot et al., 2003). However, more attention has been paid to climate change over monsoon areas (e.g., Zhao et al., 2007; Ohgaito and Abe-Ouchi, 2009; Jiang et al., 2012, 2013a; Tian and Jiang, 2018) and large-scale circulations (e.g., Zhou and Zhao, 2010, 2013). Ocean and vegetation feedbacks of this period on monsoon precipitation are also concerned (Tian and Jiang, 2013, 2015; Wang and Wang, 2013). How the MH ACA's climate changes in the PMIP multimodels is still unclear.

The Last Glacial Maximum (approximately 21,000 calendar years ago, LGM) was the last glacial interval during the Quaternary period, which is another focus period in the PMIP (Braconnot et al., 2003). During the LGM, large ice sheets covered northern Europe and North America, and the greenhouse gas concentration was much lower than the current concentration. Many proxy data-based studies suggest strong cooling and drier conditions occurred in this period relative to that under the PI climate (Bartlein et al., 2011). The mean surface temperature had an estimated cooling of 3–8°C over the land (Holden et al., 2010; Annan and Hargreaves, 2013) and 0.7–2.7°C over the ocean (MARGO Project Members, 2009; Wang T et al., 2013). Regionally, natural archives show drier climate over East and Central Asia (Yu et al., 2000; Herzschuh, 2006; Huang, 2011; Yang et al., 2012; Li and Morrill, 2013; Li and Song, 2014; Zhang et al., 2018b), and Southeast Asia (DiNezio and Tierney, 2013). The current models can reproduce the strong cooling and decreased precipitation over the East Asian monsoon area well (Jiang et al., 2011; Tian and Jiang, 2016), as well as the weakened summer monsoon circulation (Jiang and Lang, 2010). Recently, Liu et al. (2018) investigated global moisture conditions and further indicated various combinations in causing regional moisture changes during the

LGM. The northern westerlies, which have important influences on the ACA climate, are also investigated by using PMIP output (Wang et al., 2018). It is suggested that the LGM high tropospheric jet shifts poleward. Nevertheless, the issues of how the PMIP multimodel simulates the LGM ACA's temperature and precipitation and which factors play a more important role in determining the moisture conditions need further investigation.

Therefore, in this study, we mainly investigated the simulated climate changes over ACA during the MH and LGM by using the multimodel results from the third phase of the PMIP (PMIP3). We focus on the following issues: can PMIP3 models reproduce modern climatology over Central Asia and Xinjiang? What are the simulated climate changes over ACA during the MH and LGM within the PMIP3? Which factors are more important in determining the moisture conditions of ACA during the typical warm and cold periods? Are the simulations consistent with the reconstructions? The remainder of this paper is organized as follows: Section 2 describes the data and methods employed in this study; Section 3 evaluates the models' performances in simulating the modern climate over ACA; In Section 4, the simulated climate changes over ACA during the MH and LGM are analyzed, focusing on surface air temperature (SAT), precipitation, and moisture conditions, and a model-data comparison is further carried out in this section. Finally, the discussions and conclusions are presented in Section 5 and Section 6, respectively.

2 Data and Methods

2.1 Model outputs, observations and reconstructions

In this study, we mainly focus on the climate changes over the core zone of arid Central Asia (ACA), including Central Asia (35°–50°N, 50°–75°E, the large rectangle in Fig. 1) and Xinjiang area in China (40°–50°N, 75°–95°E, the small rectangle in Fig. 1). Central Asia includes five countries: Kazakhstan, Kyrgyzstan, Tajikistan, Turkmenistan, and Uzbekistan. The multimodel results from the PI, MH, and LGM experiments within the framework of PMIP3 are analyzed in the present study. The detailed information on related boundary conditions of these experiments is listed in Table 1. Eight models, including three coupled atmosphere-ocean-vegetation (AOV) models and five coupled atmosphere-ocean (AO) models, were used to carry out these three experiments within the PMIP3. Model information can be found in Table 2 (more detail is available at http://pmip3.lsce.ipsl.fr/). The last 100-year simulations for each model are analyzed in this study.

Table 1 PMIP3 boundary conditions for the PI, MH and LGM experiments (http://pmip3.lsce.ipsl.fr/).

Boundary Conditions	PI	MH	LGM
Orbital parameters	[ecc = 0.016724] [obl = 23.446°] [peri – 180° = 102.04°]	[ecc = 0.018682] [obl = 24.105°] [peri – 180° = 0.87°]	[ecc = 0.018994] [obl = 22.949°] [peri – 180° = 114.42°]
Solar constant	1365 W/m^2	Same as in the PI	Same as in the PI
Date of vernal equinox	March 21 at noon	Same as in the PI	Same as in the PI
Greenhouse gases	[CO_2 = 280 ppm] [CH_4 = 760 ppb] [N_2O = 270 ppb]	[CO_2 = 280 ppm] [CH_4 = 650 ppb] [N_2O = 270 ppb]	[CO_2 = 185 ppm] [CH_4 = 350 ppb] [N_2O = 200 ppb]
Vegetation	Fixed at present state in AO or interactive AOV models	Prescribed or interactive as in PI	Same as in the PI
Ice sheets	Modern	Same as in the PI	Ice sheet extent and sea level changes as described on PMIP3 website
Topography and coastlines	Modern	Same as in the PI	Land–sea mask and elevation changes as described on PMIP3 website

Table 2 Eight models within the PMIP3.

	Model	Country	Atmosphere Resolution	Length of data			Reference
				PI	MH	LGM	
M1	CCSM4	USA	1.25° × ~0.9° L26	501	301	101	(Gent et al., 2011)
M2*	CNRM-CM5	France	~1.4° × 1.4° L31	850	200	200	(Voldoire et al., 2013)
M3^V	FGOALS-g2	China	~2.8° × 3–6° L26	700	735	100	(Li et al., 2013)
M4*	GISS-E2-R	USA	2.5° × 2° L40	1200	100	100	(Shindell et al., 2013)
M5*^{V}	IPSL-CM5A -LR	France	3.75° × ~1.9° L39	1000	500	200	(Dufresne et al., 2013)
M6*^{V}	MIROC-ESM	Japan	~2.8° × 2.8° L80	630	100	100	(Watanabe et al., 2011)
M7	MPI-ESM-P	Germany	1.875° × ~1.9° L47	1156	100	100	(Giorgetta et al., 2013)
M8*	MRI-CGCM3	Japan	1.125° × ~1.1° L48	500	100	100	(Yukimoto et al., 2012)

v denotes coupled atmosphere–ocean–vegetation (AOV) model.
* denotes the model that can calculate Penman–Monteith PET.

Together with the observed precipitation and SAT (1901–2000) from the Climatic Research Unit (CRU) dataset (Mitchell and Jones, 2005), the multimodel results from the PI experiment are used to assess the models' performances in simulating the modern ACA climate. In addition, these data are also used as the baseline climate. Multimodel median (MMM) is adopted in the following analysis to avoid the possible influence of outliers on the multimodel ensemble mean (Gleckler et al., 2008). In this study, the MMM of the differences between the MH/LGM climate and the baseline climate are used to investigate the simulated climate changes over ACA during the MH and LGM periods. Simulated and observed data are interpolated to a resolution of 1.5°×1.5° using bilinear approach (from low resolution to high resolution) or local area averaging (from high resolution to low resolution).

To further verify the simulated climate changes during the MH, we refer to the abundance of recent proxy records for ACA. Among them, the records that clearly indicate changes in precipitation or moisture during the MH are used to compare with the simulations (see Table 3, which is summarized from Chen et al. (2020)). In addition, the limited proxy records summarized by Jiang et al. (2015b) and Li and Morrill (2013) are also used to carry out model-data comparisons of the LGM ACA climate.

Table 3 Proxy records in the ACA for the MH, summarized from Chen et al. (2020).

Site name	Latitude (°N)	Longitude (°E)	Moisture condition at MH	Proxies used	References
Lake Issyk-kul	42.50	77.10	Wetter	$\delta^{18}O$, $CaCO_3$, pollen	Rasmussen et al., 2001; Ricketts et al., 2001; Ferronskii et al., 2003
Lake Bosten	41.94	86.76	Drier	Pollen	Wünnemann et al., 2006; Huang et al., 2009
Lake Akkol	50.38	89.42	Wetter	Pollen	Blyakharchuk et al., 2007
Lake Wulungu	47.20	87.29	Drier	Grain size, pollen	Liu et al., 2008
Aral Sea	45.00	60.00	Drier	Terrace, historical documents	Krivonogov et al., 2010
Lake Balikun	43.62	92.77	Drier	Pollen	Tao et al., 2010; An et al., 2012
Lake Sayram	41.5	81.03	Drier	Pollen	Jiang et al., 2013
Lake Achit Nur	49.42	90.52	Wetter	Pollen	Sun et al., 2013
Lake Aibi	45.01	82.86	Drier	Pollen	Wang W et al., 2013
Chaiwobu Peatland	43.49	87.93	Drier	Cellulose $\delta^{13}C$ value	Hong et al., 2014
Caspian Sea	41.93	50.67	Drier	Pollen	Leroy et al., 2014
Lake Bayan Nur	49.98	93.95	No change	Pollen	Tian et al., 2014
Kansu section	43.43	83.92	Drier	Magnetic proxies	Chen et al., 2016
Lujiaowan section	43.97	85.34	Drier	Magnetic proxies	Chen et al., 2016
Zeketai section	43.53	83.3	Drier	Magnetic proxies	Chen et al., 2016
Zhongliang section	43.5	87.33	Drier	Magnetic proxies	Chen et al., 2016
Kesang Cave	42.87	81.75	Drier	$\delta^{18}O$, trace element	Cheng et al., 2016; Cai et al., 2017
Ton Cave	38.40	67.34	Drier	$\delta^{18}O$, trace element	Cheng et al., 2016
Lake Lup Nur	40.00	91.00	Wetter	Grain-size, pollen, ostracod, soluble salt	Liu et al., 2016
TLSH Peatland	48.81	86.92	Drier	Pollen, *n*-alkane	Zhang et al., 2016, 2018
NRX peatland	48.8	89.9	Drier	Pollen	Feng et al., 2017
Bayanbulak Basin	42.95	84.00	Drier	Grain-size, magnetic susceptibility, loss on ignition	Long et al., 2017
Lake Kanas	48.70	87.01	Drier	Pollen	Huang et al., 2018
Baluke Cave	42.43	84.73	Drier	$\delta^{18}O$, trace element	Liu et al., 2019, 2020
YE section	37.6	55.43	Drier	$\delta^{13}C$	Wang et al., 2020
Kelashazi peat	48.11	88.36	Drier	Pollen	Wang and Zhang, 2019

2.2 Estimation of terrestrial moisture conditions

The aridity index (AI) is defined as the ratio of annual precipitation (P) to annual potential evapotranspiration (PET) (Middleton and Thomas, 1997):

$$\mathrm{AI} = \frac{\mathrm{P}}{\mathrm{PET}}. \quad (1)$$

Actual evapotranspiration (AET) includes the transpiration of plants and evaporation of the soil surface. Quantitatively, PET is equal to the amount of AET from the vegetated soil surface with adequate water.

PET can reflect the water demand of the atmosphere, and P can represent the water supply to the vegetated soil surface. Thus, their ratio can quantify the amount of water that remains in the vegetated soil surface, that is, terrestrial moisture conditions (Middleton and Thomas, 1997). According to Middleton and Thomas (1997), drylands are defined as areas with an AI<0.65. The four subtypes of drylands are hyperarid (AI<0.05), arid (0.05≤AI<0.20), semiarid (0.20≤AI<0.50), and dry subhumid (0.50≤AI<0.65).

The Penman-Monteith (PM) equation (Penman and Keen, 1948; Monteith, 1965), combining energetic drivers (e.g., radiation and near-surface air temperature) with atmospheric drivers (e.g., vapor pressure deficit and surface wind speed), is widely used to estimate PET (Fisher et al., 2011). Specifically, the Food and Agriculture Organization (FAO) of the United Nations recommends it as a standard method and provides guidelines for calculating crop water requirements (Allen et al., 1998). Monthly mean near-surface air temperature, daily-maximum/minimum air temperatures, wind speed, specific humidity, air pressure, and radiation flux are used to estimate PM PET. However, only five PMIP3 models contain all the variables in the PM PET equation. FAO PM PET can be derived as follows (Allen et al., 1998):

$$\mathrm{PET}=\frac{0.408\Delta\left(\mathrm{R_n}-\mathrm{G}\right)+\gamma\frac{900}{\mathrm{T_{mean}}+273}\mathrm{U}\left(\mathrm{e_s}-\mathrm{e_a}\right)}{\Delta+\gamma\left(1+0.34\mathrm{U}\right)}, \tag{2}$$

where U is the wind speed at 2 m (m/s); the (R_n−G) term represents the available energy (AE), determined by the surface net radiation (R_n; MJ/m^2/d) and soil heat flux density (G; MJ/m^2/d); T_{mean} is the mean daily air temperature at 2 m (℃), derived from the average of daily-maximum and daily-minimum air temperatures; the (e_s−e_a) term is the saturation vapor pressure deficit, derived from the difference between saturation vapor pressure (e_s; kPa) and actual vapor pressure (e_a; kPa, calculated from e_s and relative humidity (RH)); Δ is the slope vapor pressure curve (kPa/℃), calculated from T_{mean}; γ is the psychrometric constant (kPa/℃), calculated from surface pressure. Radiation in MJ/m^2/d is converted to equivalent evaporation in mm/d. The basis of conversion is as follows:

$$\begin{aligned}\text{Equivalent evaporation [mm/d]} &\approx \frac{\text{Radiation[MJ/m}^2\text{/d]}}{\lambda\rho_w} \\ &\approx 0.408\times\text{Radiation[MJ/m}^2\text{/d]}\end{aligned}, \tag{3}$$

where latent heat of vaporization λ=2.45 MJ/kg and density of water ρ_w=1000kg/m^3.

To avoid the uncertainty of PM PET derived from only five models, the Hargreaves (HG) PET (Hargreaves and Samani, 1985) is also calculated in this study. This equation is also recommended by FAO when data are insufficient to calculate the PM PET (Allen et al., 1998; Liu et al., 2018). Monthly mean 2 m daily maximum and minimum air temperatures are used to calculate the HG PET. Thus, the HG PET is calculated for all eight models. The equation can be written as follows:

$$\mathrm{PET}=0.0023\times\left(\mathrm{T_{mean}}+17.8\right)\times\left(\mathrm{T_{max}}-\mathrm{T_{min}}\right)^{0.5}\mathrm{R_a}, \tag{4}$$

where R_a is the extraterrestrial radiation (mm/d) with conversion of equation (3); T_{max} and T_{min} are daily maximum and daily minimum air temperatures (°C), respectively; and T_{mean} is the average of T_{max} and T_{min}. The area of agreement between PM and HG functions is emphasized in the following analysis.

3 Model Evaluation

First, we assessed the multimodel performance in simulating the modern climate over ACA. As shown in Fig. 2, the PMIP3 MMM of the annual and seasonal SAT is consistent with observations at the large scale, such as relatively high SAT over the core zone of ACA and low SAT over the plateaus and mountains (i.e., Tianshan Mountain and Altai Mountain). However, model biases exist. Positive SAT anomalies are evident over high-latitude Central Asia, whereas negative anomalies are evident over low-latitude Central Asia, most regions of Xinjiang, and the Qinghai-Tibet Plateau. In winter, the model biases are relative larger (Fig. 2o). On average, the model biases for the Central Asian area are 0.09°C, −0.24°C, 0.35°C, −0.31°C, and 0.91°C for the annual mean, spring, summer, autumn, and winter, respectively; correspondingly, those for the Xinjiang area are 0.20°C, −0.86°C, 0.03°C, −0.82°C, and 2.14°C. Different external forcings (e.g., solar radiation and GHGs) between the PI simulations and modern conditions can partly explain those model biases over ACA (Folland et al., 2001). In addition, the deficit of the models is one of the most important factors to causing these model biases.

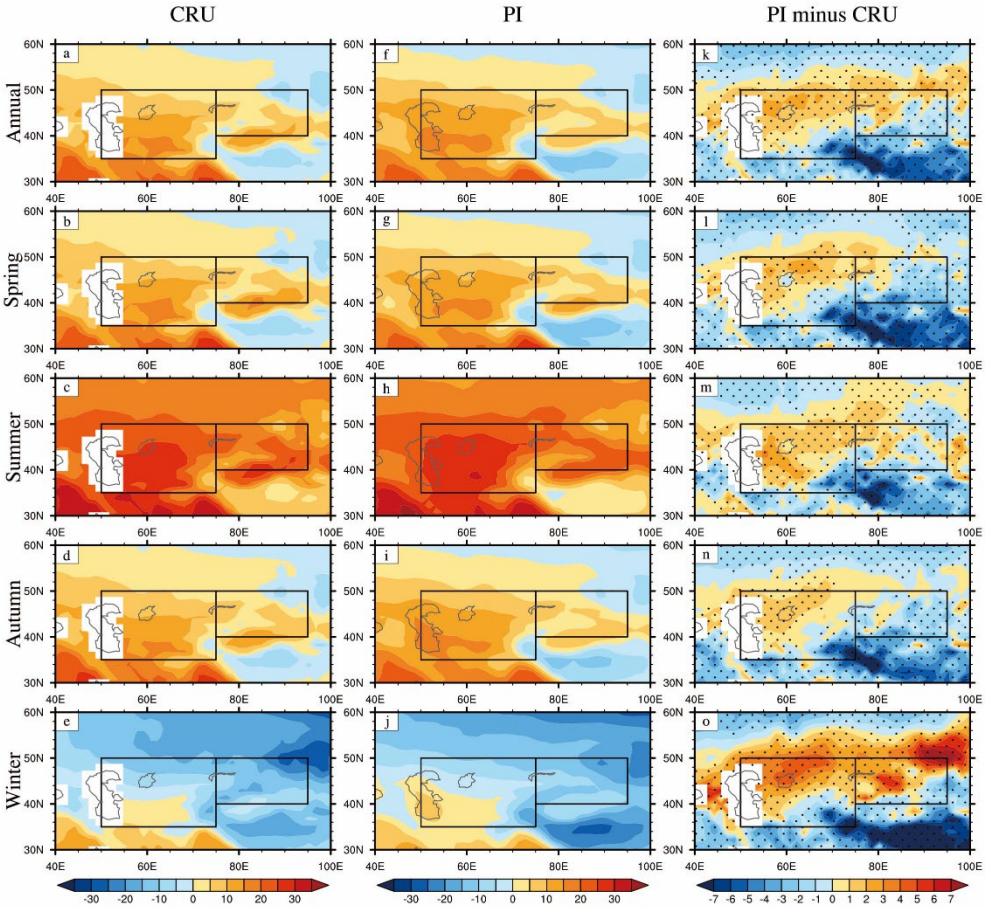

Fig. 2. Observed SAT (unit: °C) for (a) annual mean, (b) spring, (c) summer, (d) autumn, and (e) winter based on CRU data in the period of 1901–2000; The MMM of simulated SAT (unit: °C) for (f) annual mean, (g) spring, (h) summer, (i) autumn, and (j) winter based on the PMIP3 PI simulations; And (k–o) the corresponding differences in SAT between the MMM and observation. Dots in (k–o) denote that at least 5 out of 8 models agree on the sign of MMM's biases.

The simulated large-scale precipitation patterns are generally consistent with the observations, such as less precipitation in Central Asia and Xinjiang area of China, and more precipitation over the Tianshan Mountain and Tibet-Pamir Plateau (Fig. 3). However, the simulations overestimate precipitation over the mountains and around the plateaus (i.e., western Tianshan Mountain, Pamir Plateau and northern Tibetan Plateau). For ACA, the model biases are also larger in the winter than in the other seasons (Fig. 3o). Positive anomalies are evident over most parts of ACA. Quantitatively, the biases averaged over Central Asia are 0.26 mm/d, 0.27 mm/d, 0.15 mm/d, 0.29 mm/d, and 0.35 mm/d for the annual mean, spring, summer, autumn, and winter, respectively. Correspondingly over Xinjiang area, they are 0.28 mm/d, 0.30 mm/d, 0.17 mm/d, 0.25 mm/d, and 0.35 mm/d.

In addition, the MMM's performance in reproducing the seasonal cycles of regionally averaged SAT over Central Asia and Xinjiang are shown in Fig. 4a and 4b, respectively. In the observations, the higher SAT occurs in June-August (highest in July), while the lower SAT occurs in December-February (lowest in January) in both regions. The MMM of the PI simulations captures these observed characteristics of the SAT over ACA well.

For regionally averaged precipitation, in the observations, the seasonal cycle shows different characteristics between Central Asia and Xinjiang (Fig. 4c and 4d). Greater (less) precipitation can be observed in December-May (June-September) over Central Asia. Thus, the rainy seasons in Central Asia are spring and winter. In contrast, the rain seasons in the Xinjiang area occur in late spring (i.e., May) and summer (June-August), which is similar to those in the Asian monsoon area. The MMM of the PI simulations reproduces similar seasonal cycles of precipitation as those in the observation, but it overestimates the monthly mean precipitation over both Central Asia and the Xinjiang area.

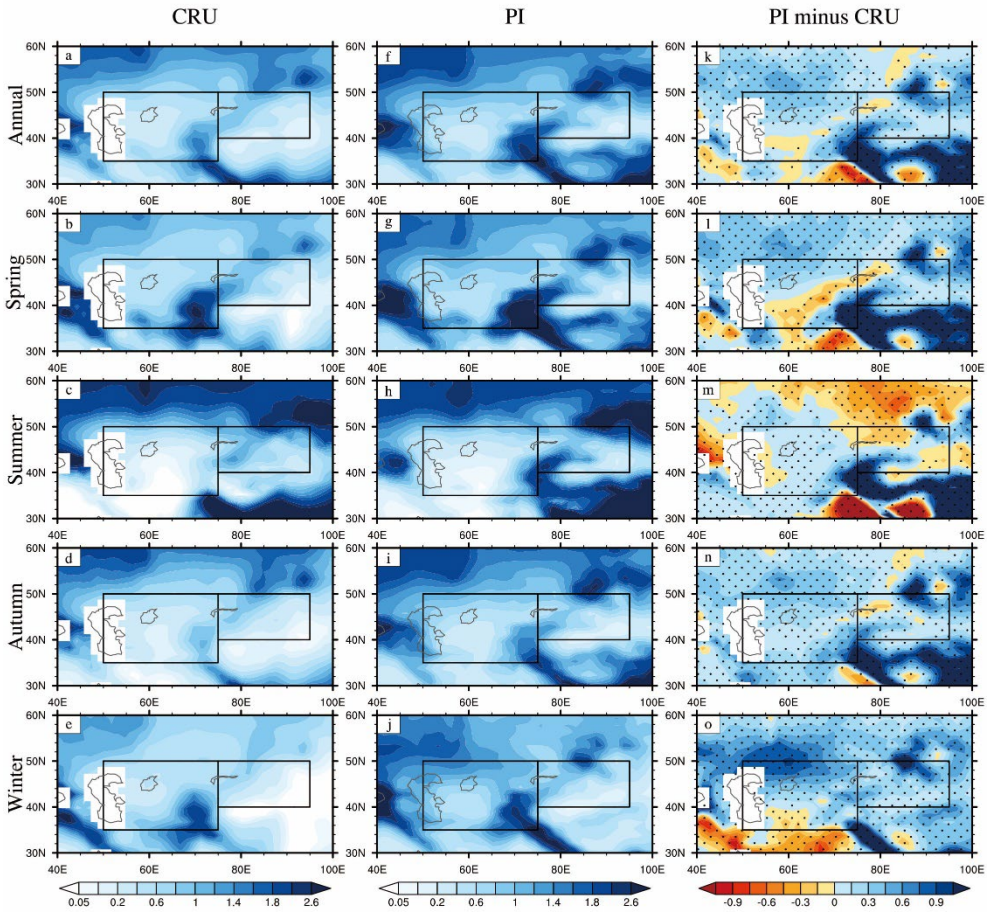

Fig. 3. Observed precipitation (unit: mm/d) for (a) annual mean, (b) spring, (c) summer, (d) autumn, and (e) winter based on CRU data in the period of 1901–2000; The MMM of simulated precipitation (unit: mm/d) for (f) annual mean, (g) spring, (h) summer, (i) autumn, and (j) winter based on the PMIP3 PI simulations; And (k–o) the corresponding differences in precipitation between the MMM and observation. Dots in (k–o) denote that at least 5 out of 8 models agree on the sign of the MMM's biases.

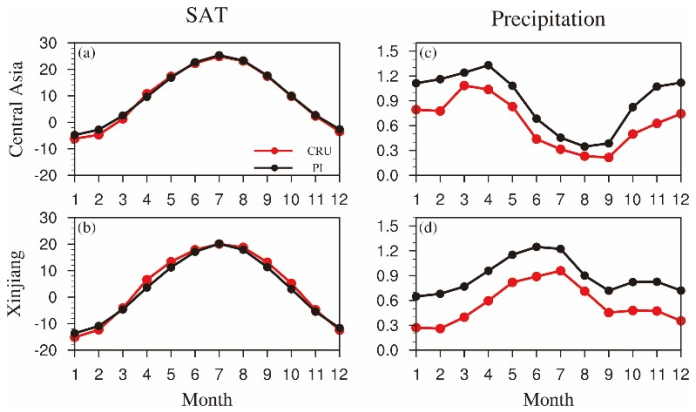

Fig. 4. The observed and MMM of simulated annual cycle of SAT (unit: °C) over the (a) Central Asia (35–50°N, 50–75°E) and (b) Xinjiang (40–50°N, 75–95°E) based on the CRU data and PMIP3 PI simulations. (c-d) Same as (a–b) but for the precipitation (unit: mm/d).

Overall, the MMM can reproduce the spatial pattern and seasonal cycle of the current ACA's SAT and precipitation reasonably well. It is a good starting point to address issues related to changes in ACA climate during the MH and LGM.

4 Results

4.1 Simulated changes in SAT and precipitation during the MH and LGM

4.1.1 SAT

During the MH, the simulated SAT shows significant differences from that during the PI (Fig. 5f-5j). The annual mean SAT decreases over most parts of the ACA region. The regionally averaged MMM decreases by 0.13°C compared to the PI, and 5 out of 8 models reproduce the lower SAT during the MH (Fig. 5f; Table 4). Additionally, a stronger decrease in SAT is evident in the MH spring and winter than in the MH autumn and summer, particularly over Kazakhstan and China's Xinjiang area. The regionally averaged SAT over the core zone of ACA decreases by 1.23°C and 1.11°C in the spring and winter, respectively. For the Xinjiang area, the SAT decreases by 1.44°C in the spring and 1.21°C in the winter, which are greater decreases than those in Central Asia. In contrast, in the MH summer, the SAT increases significantly almost throughout the entire area, with a 2.03°C increase over Xinjiang and a 1.51°C increase over Central Asia. Therefore, the seasonal cycle of the SAT over ACA is intensified during the MH. This scenario is mainly caused by the intensified seasonal cycle of insolation in the NH due to changes in orbital parameters (Berger, 1978). In the MH autumn, simulated changes of SAT are relatively smaller than those in the other seasons. Negative anomalies are evident over some northern parts of ACA, which are surrounded by the positive anomalies (~0.5°C).

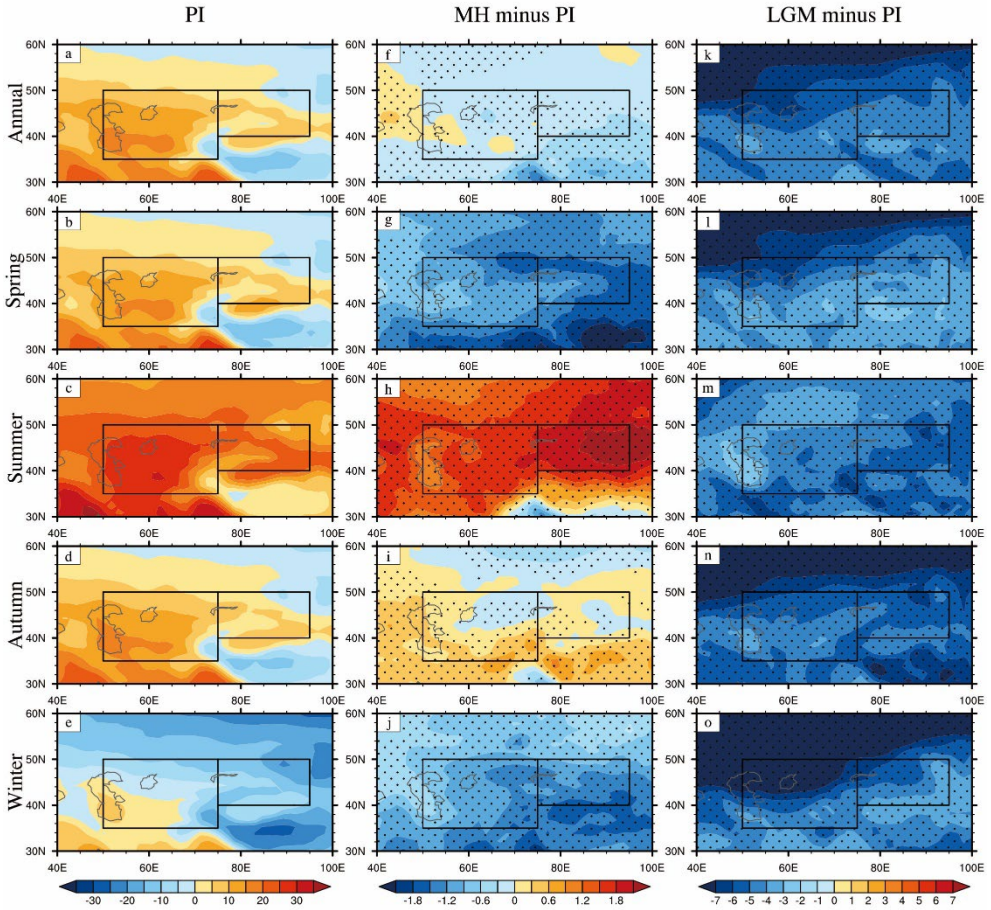

Fig. 5. (a–e) The MMM of simulated annual and seasonal mean SAT (unit: °C) based on the PMIP3 PI simulations. The MMM of simulated changes in annual and seasonal mean SAT (unit: °C) for the (f–j) MH and (k–o) LGM simulations with relative to the PI simulation. Dots in (f–o) denote that at least 5 out of 8 models agree on the sign of the MMM.

Table 4 The regionally averaged SAT (unit: °C) over the Central Asia, the Xinjiang area of China, and the core zone of ACA (i.e., Central Asia and Xinjiang) in the PI; And the regionally averaged changes in SAT (unit: °C) over above-mentioned regions for the MH and LGM with relative to the PI.

	Model	Central Asia			Xinjiang			Core zone of ACA		
		PI	MH-PI	LGM-PI	PI	MH-PI	LGM-PI	PI	MH-PI	LGM-PI
	M1	10.83	-0.38	-5.24	3.55	-0.55	-5.23	8.53	-0.43	-5.24
	M2	8.64	0.26	-2.48	1.13	0.15	-2.15	6.27	0.23	-2.38
	M3	7.99	-0.74	-5.48	0.90	-0.78	-4.42	5.74	-0.75	-5.15
	M4	9.91	0.12	-8.09	4.73	-0.17	-7.91	8.27	0.03	-8.04
Annual	M5	8.48	0.18	-5.82	1.47	0.20	-5.39	6.26	0.19	-5.69
	M6	14.05	-0.63	-7.22	6.18	-0.68	-8.07	11.56	-0.65	-7.49
	M7	11.17	-0.03	-4.64	4.54	-0.02	-3.91	9.07	-0.03	-4.41
	M8	9.58	-0.02	-3.90	3.25	-0.18	-3.41	7.58	-0.07	-3.74
	MMM	9.96	-0.11	-5.13	3.30	-0.18	-4.83	7.85	-0.13	-5.04
	M1	10.02	-1.38	-4.39	3.96	-1.90	-4.45	8.10	-1.55	-4.41
	M2	8.22	-0.93	-2.92	1.90	-1.38	-2.83	6.22	-1.07	-2.89
	M3	6.94	-2.10	-4.09	-0.60	-1.86	-2.90	4.55	-2.02	-3.72
	M4	9.39	-0.61	-8.97	4.04	-1.16	-7.18	7.69	-0.78	-8.40
Spring	M5	7.58	-0.88	-5.40	1.04	-1.18	-4.74	5.51	-0.98	-5.19
	M6	13.47	-2.00	-7.99	5.00	-3.26	-9.87	10.79	-2.39	-8.59
	M7	11.68	-0.88	-4.53	6.11	-1.31	-3.09	9.91	-1.01	-4.08
	M8	10.03	-1.06	-3.99	4.04	-1.38	-3.24	8.14	-1.16	-3.75
	MMM	9.63	-1.13	-4.51	3.53	-1.44	-4.03	7.70	-1.23	-4.36
	M1	25.08	1.35	-4.76	19.95	1.80	-5.89	23.45	1.49	-5.12
	M2	23.22	1.84	-0.89	18.04	2.38	-1.32	21.58	2.01	-1.02
	M3	23.32	1.01	-5.02	17.66	1.25	-4.66	21.53	1.08	-4.91
	M4	19.32	0.68	-6.15	16.68	0.95	-8.89	18.48	0.77	-7.02
Summer	M5	21.96	1.57	-5.39	16.26	2.18	-5.36	20.16	1.76	-5.38
	M6	27.32	1.23	-6.08	22.54	2.58	-8.71	25.81	1.66	-6.91
	M7	23.87	1.61	-3.85	18.25	2.17	-4.51	22.09	1.78	-4.06
	M8	24.88	1.70	-2.87	19.38	1.95	-3.53	23.14	1.78	-3.08
	MMM	23.78	1.51	-4.49	18.41	2.03	-5.16	22.08	1.67	-4.70
	M1	10.89	-0.02	-4.89	3.64	-0.25	-5.21	8.60	-0.09	-4.99
	M2	9.24	0.58	-2.46	0.65	0.56	-2.28	6.52	0.57	-2.40
	M3	7.89	-0.09	-5.78	1.18	-0.44	-5.64	5.76	-0.20	-5.74
	M4	10.49	0.37	-6.72	5.02	0.05	-7.93	8.76	0.27	-7.10
Autumn	M5	8.65	0.56	-5.83	1.02	0.47	-6.02	6.23	0.53	-5.89
	M6	13.37	-0.15	-6.39	6.07	-0.09	-7.23	11.06	-0.13	-6.66
	M7	11.56	0.13	-4.35	4.37	0.21	-4.18	9.28	0.16	-4.30
	M8	8.70	0.25	-3.80	2.26	-0.07	-3.40	6.66	0.15	-3.67
	MMM	9.98	0.17	-5.05	3.04	0.04	-5.27	7.78	0.13	-5.12
	M1	-2.64	-1.48	-6.95	-13.36	-1.88	-5.41	-6.04	-1.61	-6.46
	M2	-6.12	-0.43	-3.65	-16.07	-0.93	-2.17	-9.27	-0.59	-3.18
	M3	-6.18	-1.77	-7.04	-14.63	-2.10	-4.50	-8.86	-1.88	-6.23
	M4	0.42	0.03	-10.51	-6.84	-0.51	-7.65	-1.88	-0.14	-9.61
Winter	M5	-4.27	-0.54	-6.68	-12.41	-0.66	-5.46	-6.85	-0.58	-6.29
	M6	2.00	-1.59	-8.38	-8.91	-1.95	-6.44	-1.45	-1.70	-7.77
	M7	-2.45	-1.00	-5.85	-10.59	-1.14	-3.87	-5.03	-1.04	-5.22
	M8	-5.29	-0.97	-4.96	-12.67	-1.23	-3.45	-7.62	-1.05	-4.48
	MMM	-3.39	-1.06	-6.34	-12.10	-1.21	-4.88	-6.15	-1.11	-5.88

During the LGM, the SAT decreases significantly over ACA throughout the year (Fig. 5k-5o). The cooling is amplified with the increase in latitude in all seasons except summer. This simulated

large-scale cooling is mainly caused by extensive LGM ice sheets and low GHG concentrations, which are also noted in previous studies (e.g., Braconnot et al., 2007b). Quantitatively, the regionally averaged MMM of SAT over the core zone of ACA decreases by 5.04°C, 4.36°C, 4.70°C, 5.12°C, and 5.88°C for the annual mean, spring, summer, autumn and winter, respectively (Table 4). All the models could reproduce the strong cooling throughout the year during the LGM, and the SAT decrease is in the range of 2.38–8.04°C, 2.89–8.59°C, 1.02–7.02°C, 2.40–7.10°C, and 3.18–9.61°C for the annual mean and four seasons (Table 4). The simulated surface cooling is stronger in the winter than in the other seasons.

4.1.2 Precipitation

During the MH period, the annual mean precipitation decreases significantly over most ACA regions, whereas it increases over the Tibetan Plateau south of 35°N (Fig. 6f). In the spring and summer, the precipitation anomalies show similar patterns with those of the annual mean (Fig. 6g and 6h). In winter, the precipitation increases (decreases) over the northern (southern) ACA region, which is very different from the annual mean pattern (Fig. 6j). In autumn, the precipitation anomaly pattern over the northern Central Asia is similar to that in winter (Fig. 6i). However, the precipitation increases over eastern Xinjiang and south of ACA. These increases are stronger in summer. This summer and autumn increased precipitation over the Tibetan Plateau and south of ACA suggests enhanced monsoon precipitation during the MH, as noted by Wang et al. (2010). But in summer, the precipitation decreases over the Central Asia and northern Xinjiang area, which is similar to that in spring and annual mean. Quantitatively, the MMM of precipitation averaged over the core area of ACA decreases by 3.45%, 5.77%, 5.69%, 0.39%, and 5.24% compared to that of the PI for the annual mean, spring, summer, autumn and winter, respectively (Table 5). Except for the autumn, at least 7 out of 8 models simulate decreased precipitation with the same sign of MMM. Separately, Central Asia and Xinjiang area exhibit consistent anomalous precipitation signals with those over the core area of ACA.

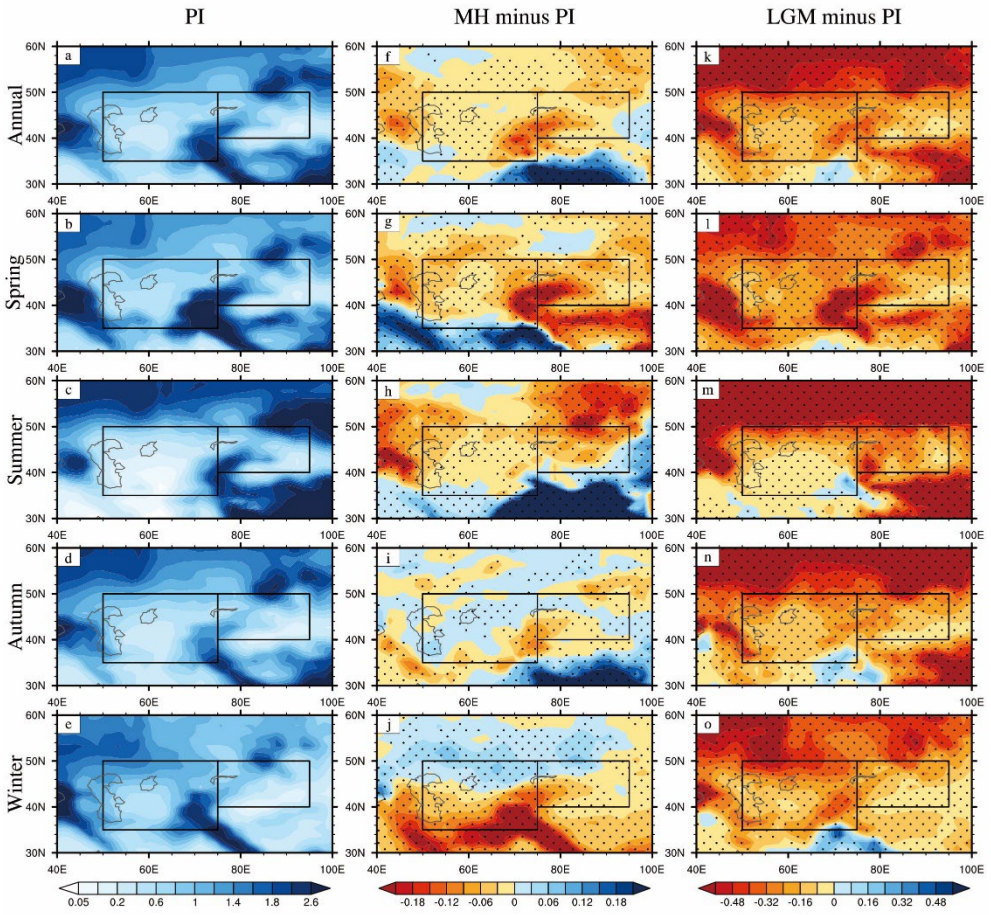

Fig. 6. (a–e) The MMM of simulated annual and seasonal mean precipitation (unit: mm/d) based on the PMIP3 PI simulations. The MMM of simulated changes in annual and seasonal mean precipitation (unit: mm/d) for the (f–j) MH and (k–o) LGM simulations with relative to the PI simulation. Dots in (f–o) denote that at least 5 out of 8 models agree on the sign of the MMM.

Table 5 The regionally averaged precipitation (unit: mm/d) over the Central Asia, the Xinjiang area of China, and the core zone of ACA (i.e., Central Asia and Xinjiang) in the PI; And the regionally averaged changes in precipitation (unit: %) over above-mentioned regions for the MH and LGM with relative to the PI.

	Model	Central Asia			Xinjiang			Core area of ACA		
		PI	MH (%) Changes	LGM (%) Changes	PI	MH (%) Changes	LGM (%) Changes	PI	MH (%) Changes	LGM (%) Changes
Annual	M1	0.93	-1.11	-32.35	0.97	2.37	-28.09	0.94	-0.01	-31.00
	M2	0.79	-3.26	-21.93	0.76	0.41	-7.97	0.78	-2.10	-17.51
	M3	1.15	-3.83	-40.28	1.03	-10.41	-42.05	1.11	-5.91	-40.84
	M4	1.48	-4.72	-23.78	1.17	5.18	-25.07	1.38	-1.59	-24.19
	M5	0.78	-2.99	6.53	0.89	-5.21	-23.59	0.81	-3.70	-3.01
	M6	1.17	-0.42	-34.84	1.41	-13.02	-41.65	1.24	-4.41	-37.00
	M7	0.67	-6.48	-17.55	0.69	-9.04	-26.53	0.67	-7.29	-20.39
	M8	0.82	-5.14	-33.29	0.75	0.37	-28.75	0.80	-3.40	-31.85
	MMM	0.91	-3.19	-27.78	0.90	-4.01	-27.77	0.91	-3.45	-27.78
Spring	M1	1.23	-2.43	-31.05	1.09	-5.59	-23.93	1.18	-3.43	-28.80
	M2	1.16	-4.72	-29.29	0.81	-10.19	-21.05	1.05	-6.45	-26.68
	M3	1.59	-3.29	-41.03	1.20	-12.44	-41.05	1.47	-6.19	-41.04
	M4	1.71	-7.89	-20.03	1.17	-6.03	-18.92	1.54	-7.30	-19.68
	M5	0.94	5.32	0.57	0.95	-4.91	-15.55	0.95	2.08	-4.53
	M6	1.64	-4.01	-28.84	1.47	-15.99	-40.18	1.59	-7.81	-32.43
	M7	0.91	-11.16	-23.52	0.70	-19.15	-39.89	0.84	-13.69	-28.71
	M8	1.17	-0.19	-34.42	0.82	-0.45	-33.51	1.06	-0.27	-34.14
	MMM	1.21	-4.14	-27.79	0.96	-9.26	-28.97	1.13	-5.77	-28.16
Summer	M1	0.46	-0.98	-39.73	1.29	0.95	-32.74	0.73	-0.37	-37.52
	M2	0.47	-2.15	-11.33	1.20	5.81	4.53	0.70	0.37	-6.31
	M3	0.62	-1.51	-46.13	0.99	-11.45	-49.28	0.73	-4.66	-47.13
	M4	0.90	-12.12	-16.33	1.25	10.92	-37.64	1.01	-4.82	-23.08
	M5	0.41	-8.01	31.41	1.02	-8.40	-29.54	0.61	-8.14	12.11
	M6	0.76	6.10	-28.92	2.04	-16.64	-45.37	1.17	-1.10	-34.13
	M7	0.34	-20.57	-26.88	0.89	-7.22	-12.87	0.52	-16.34	-22.44
	M8	0.50	-12.13	-37.61	1.01	0.73	-26.22	0.66	-8.06	-34.00
	MMM	0.50	-5.96	-32.40	1.13	-5.12	-29.74	0.70	-5.69	-31.56
Autumn	M1	0.87	9.74	-31.68	0.79	11.50	-33.91	0.85	10.30	-32.39
	M2	0.67	5.20	-24.28	0.66	9.95	-14.54	0.67	6.70	-21.20
	M3	0.99	0.46	-38.86	0.93	-2.58	-36.78	0.97	-0.50	-38.20
	M4	1.36	-3.05	-14.76	1.18	14.24	-18.20	1.30	2.43	-15.85
	M5	0.56	-8.32	40.71	0.82	-3.70	-13.22	0.64	-6.86	23.63
	M6	0.98	0.63	-51.42	1.13	-5.52	-47.75	1.03	-1.32	-50.26
	M7	0.52	1.33	-6.34	0.67	-6.32	-30.56	0.57	-1.09	-14.01
	M8	0.79	-10.02	-39.35	0.68	-2.53	-42.00	0.76	-7.65	-40.19
	MMM	0.77	-0.19	-26.39	0.79	-0.82	-30.64	0.78	-0.39	-27.74
Winter	M1	1.16	-5.88	-29.07	0.70	5.23	-17.42	1.01	-2.36	-25.38
	M2	0.85	-9.26	-19.31	0.38	-9.26	0.64	0.70	-9.26	-12.99
	M3	1.39	-9.14	-35.44	0.98	-13.80	-40.94	1.26	-10.62	-37.18
	M4	1.97	4.78	-27.39	1.08	-2.35	-21.59	1.69	2.52	-25.55
	M5	1.21	-5.27	0.47	0.76	-4.36	-35.08	1.07	-4.98	-10.79
	M6	1.29	-1.85	-24.99	1.01	-10.66	-28.01	1.20	-4.64	-25.95
	M7	0.90	-5.48	-15.70	0.51	-3.02	-27.02	0.77	-4.70	-19.28
	M8	0.83	-5.28	-24.73	0.49	5.64	-13.19	0.72	-1.83	-21.08

MMM	1.13	-5.64	-23.24	0.68	-4.35	-23.41	0.99	-5.24	-23.29

During the LGM, the precipitation decreases over most regions of ACA throughout the year (Fig. 6k-6o). Stronger negative precipitation anomalies exist over high-latitude regions in most seasons and in the annual mean. Quantitatively, the MMM of mean annual precipitation over the core area of ACA decreases by 27.78% relative to that of the PI, with a range of 3.01%–40.84%. In summer, the decrease is largest among the four seasons. The corresponding MMM is −31.38%, and the maximum decrease is larger than 40% among the models (Table 5). Less precipitation during the LGM could relate to the significant cooling, which could suppress the atmospheric moisture-holding ability and enhance regional subsidence and then weaken the hydrological cycle (Held and Soden, 2006; Quade and Broecker, 2009).

4.1.3 Simulated changes in seasonal cycle

During the MH and LGM, the simulated seasonal cycles of SAT over Central Asia and Xinjiang are similar to those of the PI (not shown). In the MH, however, regionally averaged SATs over Central Asia and Xinjiang are higher in June-September than those of the PI, whereas lower in other months (Fig. 7a and 7b). This result means that the seasonal cycles of SAT over the core area of ACA are strengthened. During the LGM, regionally averaged SATs over Central Asia and Xinjiang are 4–6°C lower than those of the PI throughout the year. The larger decreases in SAT are evident in the winter and August. Specifically, over Xinjiang, the largest LGM decrease in SAT occurs in August. Therefore, the seasonal cycles of SAT change little during the LGM. Over the Xinjiang area, the seasonal SAT cycle is slightly weakened.

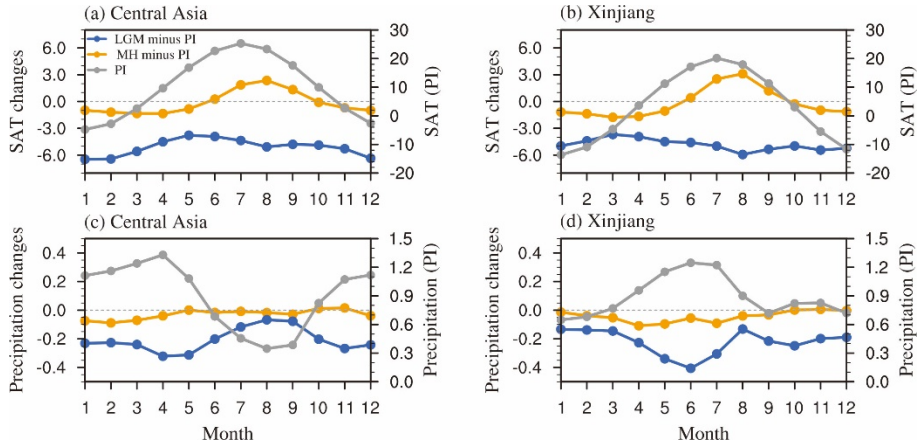

Fig. 7. The MMM of simulated changes in annual cycle of SAT (unit: °C) over the (a) Central Asia (35–50°N, 50–75°E) and (b) Xinjiang (40–50°N, 75–95°E) for the MH (orange line) and LGM (blue line) relative to that in the PI (gray line). (c-d) Same as (a–b) but for the precipitation (unit: mm/d).

Regionally averaged precipitation is reduced over Central Asia and Xinjiang during the whole year in the MH (Fig. 7c and 7d). However, the reduction is small, at no greater than 0.1 mm/d. Thus, the reduction has little influence on the seasonal cycle of precipitation over ACA during the MH. During the LGM, the reduction in regionally averaged precipitation is stronger than that during the MH. For annual evolution, a larger decrease in precipitation occurs in the boreal winter and spring over Central Asia, whereas it occurs in May, June, and July over the Xinjiang area. The evolution of precipitation reductions differ from the PI climatology for these two areas. This result suggests that seasonal cycles of LGM precipitation over Central Asia and Xinjiang are both weakened.

4.2 Simulated changes in terrestrial moisture during the MH and LGM

Terrestrial moisture conditions can be classified by AI climatology; according to Middleton and Thomas (1997), drylands are regions with AI<0.65, and smaller AI values suggest drier conditions over land. In the PI, most parts of the core region of ACA are drylands (Fig. 8a and 8b). The AI patterns calculated by the PM and HG methods are similar, both of which well represent the modern moisture condition over ACA.

4.2.1 Terrestrial moisture changes

During the MH, negative AI anomalies are evident over the southern part of Central Asia and western Xinjiang, suggesting a drier condition (Fig. 8c and 8d). For the northern part of Central Asia and eastern part of Xinjiang, multimodel simulated changes in AI show large uncertainties.

In the LGM, large-scale negative changes in AI can be found over the whole core zone of ACA and its surrounding regions (Fig. 8e and 8f). This suggests much drier conditions over ACA during this period than during the PI, even compared to that during the MH.

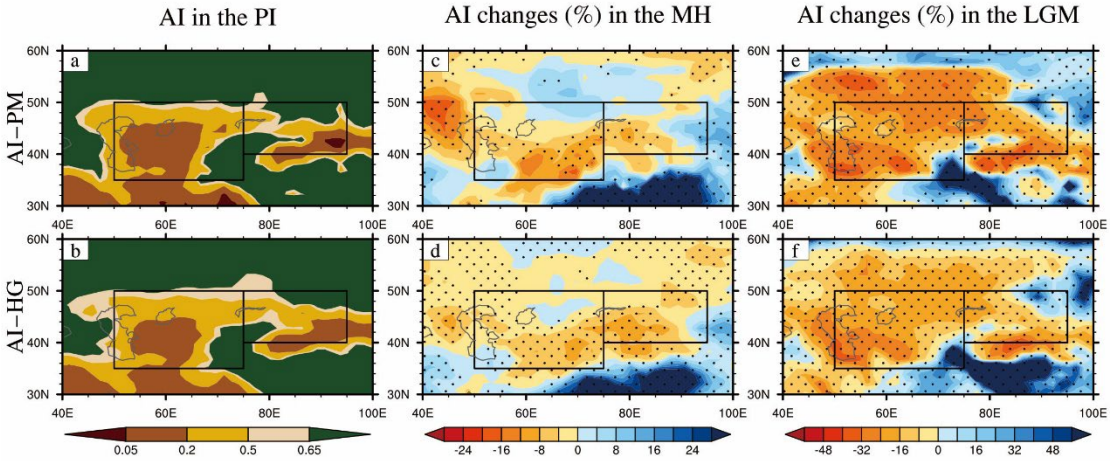

Fig. 8. (a–b) The MMM of simulated AI in the PI. The MMM of simulated changes of AI (%) for the (c–d) MH and (e–f) LGM relative to AI in the PI. Black dots denote that at least 3 out of 5 (5 out of 8) models agree on the sign of the MMM using the PM (HG) method. (a), (c), and (e) are calculated by the PM method. (b), (d), and (f) are calculated by the HG method.

To quantify the impact of precipitation and PET on changes in AI, a detailed estimation is calculated according to Feng and Fu (2013):

$$\Delta(\mathrm{AI}) \approx \frac{1}{\mathrm{PET}}\Delta\mathrm{P} - \frac{\mathrm{P}}{\mathrm{PET}^2}\Delta\mathrm{PET} + \frac{\mathrm{P}}{\mathrm{PET}^3}(\Delta\mathrm{PET})^2, \quad (5)$$

where ΔP and ΔPET are the changes in precipitation and PET, respectively. The term on the left side of equation (5) is the change in AI. On the right side of equation (5), the first term and the remaining terms represent contributions of precipitation and PET to changes in AI, respectively. For convenience, we define the following:

$$F(\Delta P) = \frac{1}{\mathrm{PET}}\Delta P, \quad (6)$$

$$G(\Delta\mathrm{PET}) = -\frac{\mathrm{P}}{\mathrm{PET}^2}\Delta\mathrm{PET} + \frac{\mathrm{P}}{\mathrm{PET}^3}(\Delta\mathrm{PET})^2. \quad (7)$$

As shown in Fig. 9a and 9b, reduced precipitation can cause a decrease of approximately 9% in AI over southern Central Asia and most parts of Xinjiang during the MH. Over Tajikistan and Uzbekistan, enhanced PET also contributes to the decrease in AI during this period (Fig. 9c and 9d). In contrast, the PET is reduced over the Xinjiang area. Its contribution is positive to the AI (~3%), which is smaller than that from precipitation. PET can only partly offset the effects of decreased precipitation on the AI changes over most parts of Xinjiang. Overall, reduced precipitation plays a dominant role in causing changes in AI over southern Central Asia and the Xinjiang area during the MH.

During the LGM, reduced precipitation leads to a decrease (~30%) of AI over ACA (Fig. 9e and 9f). At the higher latitudes in ACA, the precipitation induced changes can be as high as 40% of PI AI or more. In contrast, reduced PET can lead to an increase in AI over the whole ACA. Reduced PET can lead to an increase of more than 10% of the PI AI over ACA. As shown in Fig. 9e-9h, changes in precipitation and PET both contribute more to AI during the LGM than during the MH. However, their contributions are opposite, and precipitation is dominant. Liu et al. (2018) analyzed moisture conditions over the western Central Asia and noted similar results. Thus, the AI decreases by approximately 30% over almost all regions of ACA during the LGM (Fig. 8e and 8f).

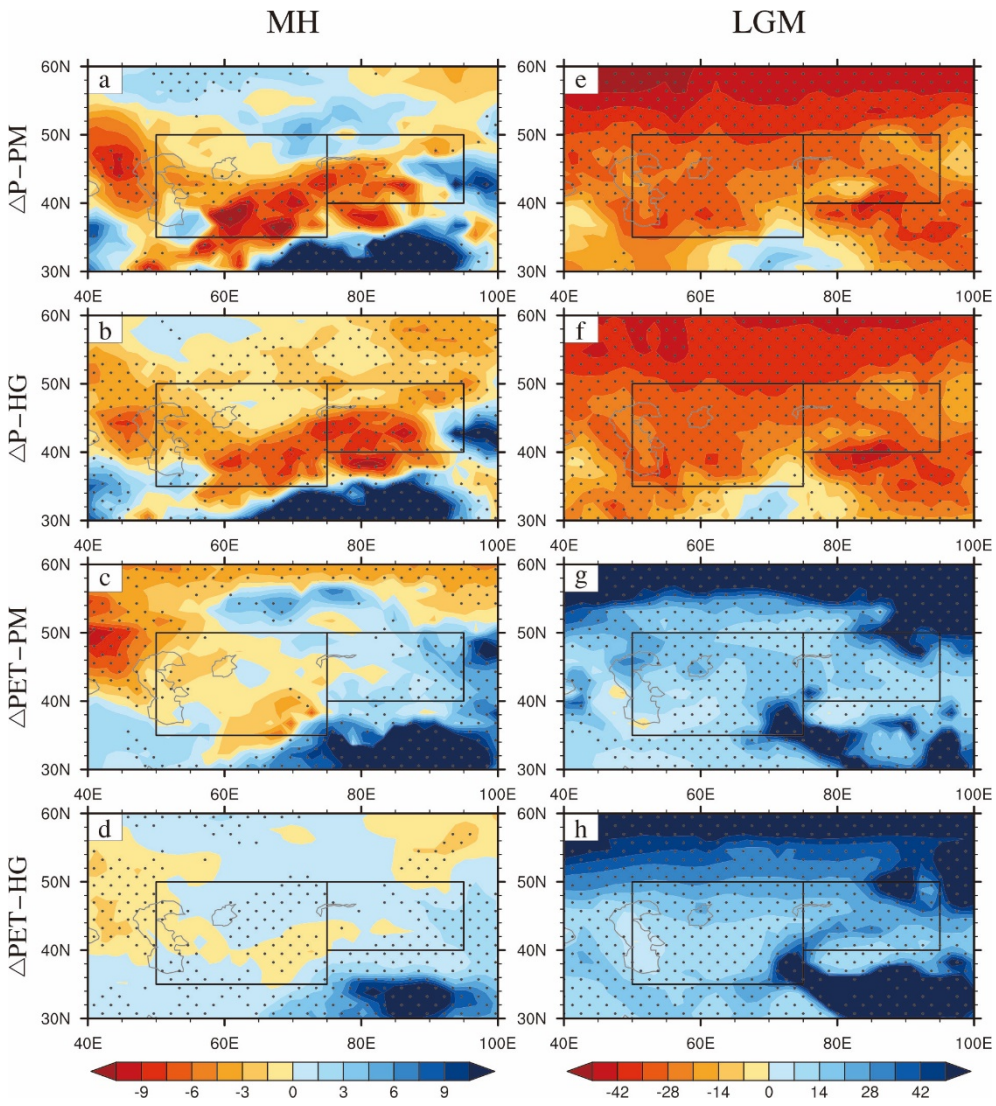

Fig. 9. The AI changes (%, relative to PI) caused by changes in (a–b) precipitation and (c–d) PET using the PM and HG methods for the MH period. (e–h) Same as (a-d), but for the LGM. Black dots denote that at least 3 out of 5 (5 out of 8) models agree on the sign of the MMM using the PM (HG) method.

4.2.2 Effects of changes in T_{mean}, RH, U, and AE

As mentioned above, changes in precipitation dominate the AI over most regions of ACA. However, influence from PET is also essential, particularly during the LGM. Therefore, it is necessary to find out the key factors influencing the PET and AI in these two periods. In equation (2), PM PET is a function of U, AE, RH, and T_{mean}. Thus, the contributions of some basic meteorological elements (i.e., U, AE, RH and T_{mean}) to PET changes can be obtained following equations in Fu and Feng (2014):

$$T_C = f(U_0, T_{mean1}, RH_0, AE_0) - f(U_0, T_{mean0}, RH_0, AE_0), \quad (8)$$

$$U_C = f(U_1, T_{mean0}, RH_0, AE_0) - f(U_0, T_{mean0}, RH_0, AE_0), \quad (9)$$

$$RH_C = f(U_1, T_{mean1}, RH_1, AE_1) - f(U_1, T_{mean1}, RH_0, AE_1), \quad (10)$$

$$AE_C = f(U_1, T_{mean1}, RH_1, AE_1) - f(U_1, T_{mean1}, RH_1, AE_0), \quad (11)$$

$$\Delta PET \approx T_C + U_C + RH_C + AE_C \quad (12)$$

where T_C, U_C, RH_C and AE_C are the contributions of T_{mean}, RH, U, and AE to changes in PET,

respectively. Subscript "0" represents the PI climatology, and subscript "1" represents the MH/LGM climatology. Substituting equation (12) into equation (7), the contributions of T_{mean}, RH, U, and AE to the AI changes will be obtained. Increasing T_{mean}, U, and AE can contribute to enhancing PET and thereby decreasing AI (drier). In contrast, an increase in RH can lead to a reduction in PET and thereby an increase in AI (wetter).

During the MH (Fig. 10), increased U is an important factor in enhancing the PET and thereby to decreasing the AI over ACA. In contrast, AE can contribute to a decrease in AI over the western core area of ACA, whereas an increases in AI over the Xinjiang area in China (Fig. 10c). It means that the AE contributes oppositely to the AI changes over the western and eastern core zone of ACA. Compared with the influences from U and AE, the influences from T_{mean} and RH are smaller and show large discrepancies among the models over the core zone of ACA (Fig. 10a and 10b).

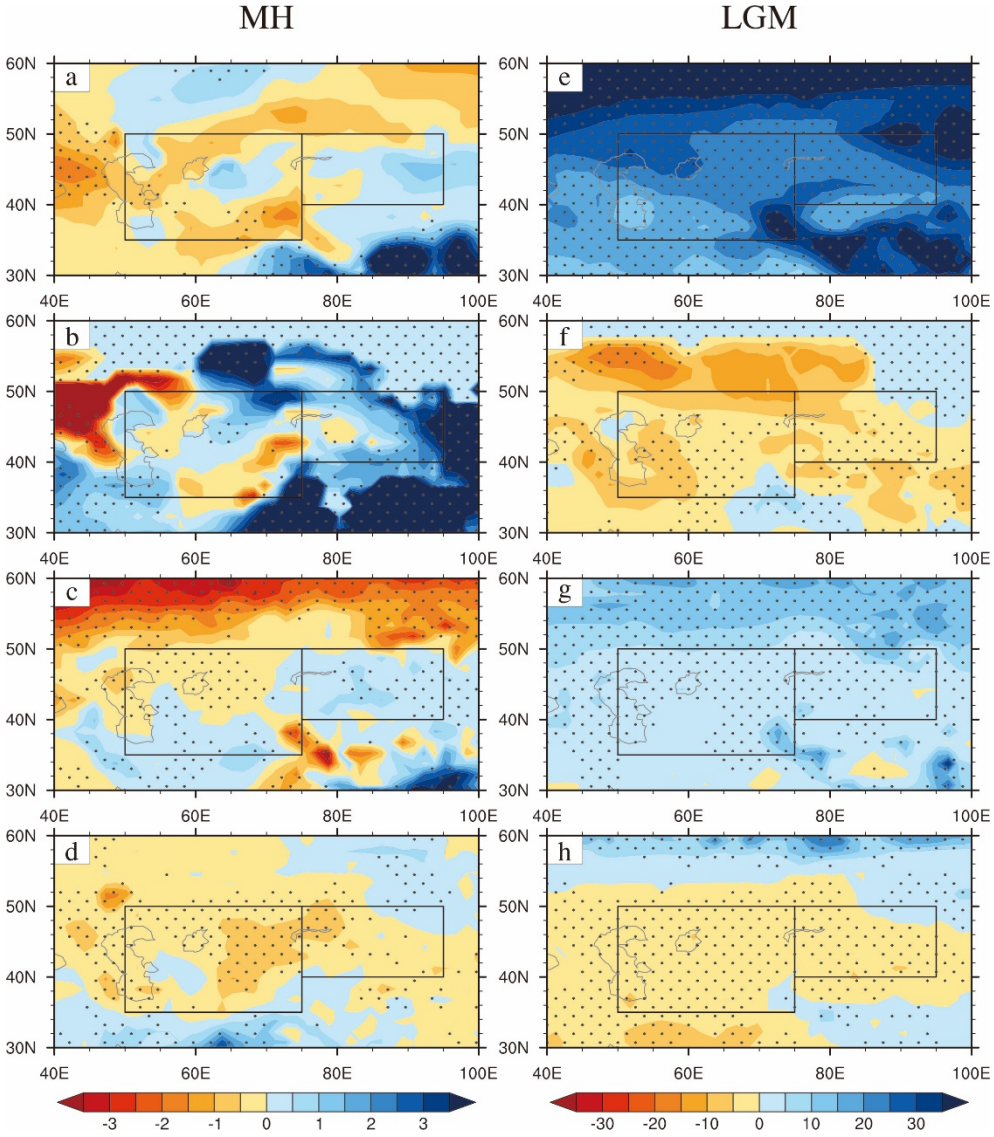

Fig. 10. The AI changes (%, relative to PI) caused by (a) Tmean, (b) RH, (c) AE, and (d) U using the PM methods for the MH period. (e–h) Same as the (a-d), but for the LGM. Black dots denote that at least 3 out of 5 models agree on the sign of the MMM.

During the LGM, remarkable cooling contributes to a significant increase in AI in Central Asia and Xinjiang area (Fig. 10e). Similarly, changes in AE also contribute to the increase in the AI during this period (Fig. 10f). In contrast, changes in RH and U contribute to the decrease in AI in the core zone of ACA, partly offsetting the influences from T_{mean} and AE (Fig. 10g and 10h). Among these four factors, the effect from the T_{mean} is largest. Similar results could be found over western part of the Central Asia in Liu et al. (2018). Compared with that in the MH, in the LGM, the contributions of T_{mean}, RH, AE, and U to the AI are much larger, even one order higher.

4.3 Model-data comparison

For the MH, as noted by our previous study (Wang et al., 2010), a significant increase in monsoon precipitation can be found over East Asia in the simulation and reconstruction. In this study, our collected proxy records are mainly located in southern Central Asia and the western Xinjiang area (Table 3, Fig. 11a). Most of the records suggest a drier condition over these regions, which is very different from that over the monsoon area. This result is consistent with the above-simulated MH ACA moisture condition. For the northern Central Asia and eastern Xinjiang areas, the simulated moisture condition is difficult to verify due to the absence of reconstructions or two model-data mismatches over these regions.

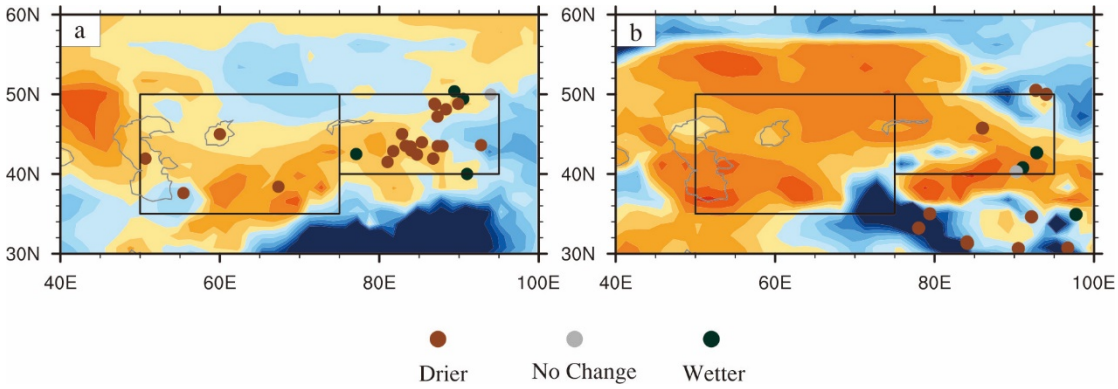

Fig. 11. Reconstructed moisture changes for the (a) MH and (b) LGM. The backgrounds of them are the changes of AI using the PM method, which are same as Fig. 8c and 8e, respectively.

For the LGM, we only find four proxy records in the core area of ACA (Fig. 11b). One record is from northern Xinjiang, and the other records are from the east edge of ACA. The proxy record in northern Xinjiang indicates a relatively drier condition, which is consistent with the simulation. However, the other three records suggest wetter or no change in their conditions over their local regions, showing opposite trends to those of the model results. In fact, the minimal records for ACA, particularly in Central Asia, limit the model-data comparison for the LGM climate over ACA, also noted by the Liu et al (2018).

5 Discussions

In the paleoclimate modelling study, reconstruction is key to verifying the model results. However, there are very large uncertainties in the proxy records. As mentioned above, proxy data derived from Overeem et al (2003), An et al (2006) and Chen et al (2008) suggest a wetter ACA during the MH. Actually, the number of these proxy records is limited. In addition, some of them are located in the eastern Xinjiang area in China, where the climate is also affected by the monsoon. The wetter conditions are exactly a reflection of a stronger East Asian summer monsoon during this period, which is consistent with our model results (Fig. 8c and 8d) and previous PMIP2 studies (e.g., Wang et al., 2010). For the western Xinjiang area and few regions of Central Asia, our collected information (Table 3) suggests likely drier conditions, further confirming the present model results. However, the recently collected information does not match reconstructed record from Overeem et al (2003). In addition, there are no reconstructed records in most parts of the Central Asia, particularly at the LGM. This makes it difficult to accurately understand related climate change. Therefore, to better study and understand the paleoclimate, we need multiple and large amounts of reconstructed data to confirm each other. Comparisons between the multi model and large reconstruction data are particularly important and necessary.

From the first phase of the PMIP to the ongoing PMIP4, the MH and LGM are always most concerned periods for paleoclimate modelling. The MH and LGM experiments are used to examine the climate response to a change in the seasonal and latitudinal distribution of incoming solar radiation as well as the presence of large ice sheets and lowered greenhouse gas concentrations, respectively (Braconnot et al., 2007a). That means these changes in external forcing are the root causes to induce climate changes over ACA during the MH and LGM. However, the related dynamical processes are still unclear. The present study only notes the final changes (i.e., changes in SAT, precipitation, and related moisture conditions) due to the forcings. The associated mechanisms will be studied in the next step.

6 Conclusions

(1) In this study, the climate changes during the MH and LGM over ACA are investigated using output from the PMIP3. MMM is adopted to avoid the possible influence of outliers on the multimodel ensemble mean. Based on the comparison between the MMM and observations, the PMIP3 model results can realistically simulate the current ACA climate.

(2) During the MH, the simulated annual SAT averaged over the core area of ACA decreases by 0.13°C. At a seasonal scale, the SAT increases by 1.67/0.13°C in summer/autumn, whereas it decreases by 1.23/1.11°C in spring/winter. The seasonal cycle is intensified, similar to the condition in the East Asian monsoon region (e.g., Wang et al., 2010). This is mainly caused by the enhanced seasonal cycle of insolation in the NH due to the altered orbital parameters during the MH. For precipitation, the simulated regionally averaged MMM over the core area of ACA decreases by 3.45%, 5.77%, 5.69%, 0.39%, and 5.24% for the annual mean and in the spring, summer, autumn, and winter, respectively. The responses of precipitation over ACA are opposite to those over the NH monsoon areas, particularly in the rainy season (e.g., Jiang et al., 2013b).

(3) In the LGM, strong cooling is evident over the whole ACA throughout the year. The simulated SAT averaged over the core zone decreases by 5.04°C, 4.36°C, 4.70°C, 5.12°C, and 5.88°C for the annual mean and in the spring, summer, autumn, and winter, respectively. This cooling condition weakens the regional, even the global hydrological cycle. Thus, the simulated regionally averaged precipitation over the core region decreases by 27.78%, 28.16%, 31.56%, 27.74%, and 23.29% for the annual mean and in the spring, summer, autumn, and winter, respectively. In addition, the seasonal cycles of precipitation over Central Asia and the Xinjiang area both weaken during the LGM.

(4) In the model, southern Central Asia and western Xinjiang have drier conditions during the MH than during the PI, which is further confirmed by our collected proxy records. Reduced precipitation plays a dominant role in causing the drier conditions. In Tajikistan and Uzbekistan, enhanced PET also contributes to the decrease in AI. In contrast, in the western Xinjiang area, reduced PET contributes negatively to the decrease in AI. Detailed analysis suggests that changes in T_{mean} and U lead to enhanced PET in Tajikistan and Uzbekistan, further intensifying the drying. In contrast, changes in RH and AE result in reduced PET, thereby reducing drying in Xinjiang.

(5) In the LGM, simulated drier conditions can be found almost over the whole core area of ACA compared to that of the PI, and these conditions were much drier than those in the MH. Significantly decreased precipitation is the main cause of the drier conditions over ACA, even over large surrounding areas. In contrast, the weakened PET, which is mainly caused by decreased T_{mean} and AE, reduced the drying intensity over the whole ACA region. A change in precipitation is still the dominant factor in determining ACA's moisture condition. For this period, the lack of proxy records limits a model-data comparison over ACA.

Acknowledgments

We sincerely thank the two anonymous reviewers for their helpful comments and suggestions to improve this manuscript. This research was supported by the National Key R&D Program of China (Grant No. 2018YFA0606403), the Strategic Priority Research Program of Chinese Academy of Sciences (Grant No. XDA20070103), the National Natural Science Foundation of China (Grants 41822502), and the CAS–PKU Joint Research Program.

References

Allen, R.G., Pereira, L.S., Raes, D., and Smith, M., 1998. Crop evapotranspiration: Guidelines for computing crop water requirements. *FAO Irrigation and Drainage Paper 56*: 1–300.

An, C.B., Feng, Z.D., and Barton, L., 2006. Dry or humid? Mid–Holocene humidity changes in arid and semi–arid China. *Quaternary Science Reviews*, 25(3–4): 351–361.

An, C.B., Lu, Y.B., Zhao, J.J., Tao, S.C., Dong, W.M., Li, H., Jin, M., and Wang, Z.L., 2012. A high-resolution record of Holocene environmental and climatic changes from Lake Balikun (Xinjiang, China): Implications for central Asia. *The Holocene*, 22(1): 43–52.

Annan, J.D., and Hargreaves, J.C., 2013. A new global reconstruction of temperature changes at the Last Glacial Maximum. *Climate of the Past*, 9(1): 367–376.

Bartlein, P.J., Harrison, S.P., Brewer, S., Connor, S., Davis, B.A.S., Gajewski, K., Guiot, J., Harrison–Prentice, T.I., Henderson, A., Peyron, O., Prentice, I.C., Scholze, M., Seppa, H., Shuman, B., Sugita, S., Thompson, R.S., Viau, A.E., Willlianms, J., and Wu, H., 2011. Pollen–based continental climate reconstructions at 6 and 21 ka: a global synthesis. *Climate Dynamics*, 37(3–4): 775–802.

Berger, A., 1978. Long–term variations of daily insolation and quaternary climatic changes. *Journal of the Atmospheric Sciences*, 35(12): 2362–2367.

Blyakharchuk, T.A., Wright, H.E., Borodavko, P.S., van der Knaap, W.O., and Ammann, B., 2007. Late Glacial and Holocene vegetational history of the Altai Mountains (southwestern Tuva Republic, Siberia). *Palaeogeography, Palaeoclimatology, Palaeoecology*, 245(3–4): 518–534.

Braconnot, P., Joussaume, S., Harrison, S., Hewitt, C., Valdes, P., Ramstein, G., Stouffer, R.J., Otto-Bliesner, B.,

and Taylor, K.E., 2003. The second phase of the Paleoclimate Modeling Intercomparison Project (PMIP II). *Clivar Exchanges*, 8(4): 19–20.

Braconnot, P., Otto-Bliesner, B., Harrison, S., Joussaume, S., Peterchmitt, J.Y., Abe-Ouchi, A., Crucifix, M., Driesschaert, E., Fichefet, T., Hewitt, C.D., Kageyama, M., Kitoh, A., Laîné, A., Loutre, M.F., Marti, O., Merkel, U., Ramstein, G., Valdes, P., Weber, S.L., Yu, Y., and Zhao, Y., 2007a. Results of PMIP2 coupled simulations of the Mid-Holocene and Last Glacial Maximum – Part 1: experiments and large-scale features. *Climate of the Past*, 3(2): 261–277.

Braconnot, P., Otto-Bliesner, B., Harrison, S., Joussaume, S., Peterchmitt, J.Y., Abe-Ouchi, A., Crucifix, M., Driesschaert, E., Fichefet, T., Hewitt, C.D., Kageyama, M., Kitoh, A., Loutre, M.F., Marti, O., Merkel, U., Ramstein, G., Valdes, P., Weber, L., Yu, Y., and Zhao, Y., 2007b. Results of PMIP2 coupled simulations of the Mid-Holocene and Last Glacial Maximum – Part 2: feedbacks with emphasis on the location of the ITCZ and mid- and high latitudes heat budget. *Climate of the Past*, 3(2): 279–296.

Cai, Y.J., Chiang, J.C.H., Breitenbach, S.F.M., Tan, L.C., Cheng, H., Edwards, R.L., and An, Z.S., 2017. Holocene moisture changes in western China, Central Asia, inferred from stalagmites. *Quaternary Science Reviews*, 158: 15–28.

Chen, F.H., Yu, Z.C., Yang, M.L., Ito, E., Wang, S.M., Madsen, D.B., Huang, X.Z., Zhao, Y., Sato, T., Birks, H.J.B., Boomer, I., Chen, J.H., An, C.B., and Wünnemann, B., 2008. Holocene moisture evolution in arid central Asia and its out–of–phase relationship with Asian monsoon history. *Quaternary Science Reviews*, 27(3–4): 351–364.

Chen, F.H., Chen, J.H., and Huang, W., 2009a. A discussion on the westerly–dominated climate model in mid–latitude Asia during the modern interglacial period *Earth Science Frontiers*, 16(6): 023–032 (in Chinese with English abstract).

Chen, F.H., Wang, J.S., Jin, L.Y., Zhang, Q., Li, J., and Chen, J.H., 2009b. Rapid warming in mid–latitude central Asia for the past 100 years. *Frontiers of Earth Science in China*, 3(1): 42–50.

Chen, F.H., Huang, W., Jin, L.Y., Chen, J.H., and Wang, J.S., 2011. Spatiotemporal precipitation variations in the arid Central Asia in the context of global warming. *Science China Earth Sciences*, 54(12): 1812–1821.

Chen, F.H., Jia, J., Chen, J.H., Li, G.Q., Zhang, X.J., Xie, H.C., Xia, D.S., Huang, W., and An, C.B., 2016. A persistent Holocene wetting trend in arid central Asia, with wettest conditions in the late Holocene, revealed by multi-proxy analyses of loess-paleosol sequences in Xinjiang, China. *Quaternary Science Review*s, 146: 134–146.

Chen, F.H., Chen, J.H., Huang, W., Chen, S.Q., Huang, X.Z., Jin, L.Y., Jia, J., Zhang, X.J., An, C.B., Zhang, J.W., Zhao, Y., Yu, Z.C., Zhang, R.H., Liu, J.B., Zhou, A.F., and Feng, S., 2019. Westerlies Asia and monsoonal Asia: Spatiotemporal differences in climate change and possible mechanisms on decadal to sub–orbital timescales. *Earth–Science Reviews*, 192: 337–354.

Chen, S.Q., Chen, J.H., Lv, F.Y., Liu, X.K., Hou, J.Z., and Chen, F.H., 2020. Holocene moisture variation in arid central Asia: Reassessment and reconciliation. In preparation.

Chen, X., Jiang, F.Q., Wang, Y.J., Li, Y.M., and Hu, R.J., 2013. Characteristics of the eco–geographical pattern in arid land of central Asia. *Arid Zone Research*, 30(3): 385–390 (in Chinese with English abstract).

Chen, Y.N., Li, Z., Fan, Y.T., Wang, H.J., and Deng, H.J., 2015. Progress and prospects of climate change impacts on hydrology in the arid region of northwest China. *Environmental Research*, 139: 11–19.

Cheng, H., Spötl, C., Breitenbach, S.F.M., Sinha, A., Wassenburg, J.A., Jochum, K.P., Scholz, D., Li, X.L., Yi, L., Peng, Y.B., Lv, Y.B., Zhang, P.Z., Votintseva, A., Loginov, V., Ning, Y.F., Kathayat, G., and Edwards, R.L., 2016. Climate variations of Central Asia on orbital to millennial timescales. *Scientific Reports*, 6(1): 36975.

DiNezio, P.N., and Tierney, J.E., 2013. The effect of sea level on glacial Indo-Pacific climate. *Nature Geoscience*, 6: 485–491.

Dufresne, J.-L., Foujols, M.-A., Denvil, S., Caubel, A., Marti, O., Aumont, O., Balkanski, Y., Bekki, S., Bellenger, H., Benshila, R., Bony, S., Bopp, L., Braconnot, P., Brockmann, P., Cadule, P., Cheruy, F., Codron, F., Cozic, A., Cugnet, D., de Noblet, N., Duvel, J.-P., Ethé, C., Fairhead, L., Fichefet, T., Flavoni, S., Friedlingstein, P., Grandpeix, J.-Y., Guez, L., Guilyardi, E., Hauglustaine, D., Hourdin, F., Idelkadi, A., Ghattas, J., Joussaume, S., Kageyama, M., Krinner, G., Labetoulle, S., Lahellec, A., Lefebvre, M.-P., Lefevre, F., Levy, C., Li, Z.X., Lloyd, J., Lott, F., Madec, G., Mancip, M., Marchand, M., Masson, S., Meurdesoif, Y., Mignot, J., Musat, I., Parouty, S., Polcher, J., Rio, C., Schulz, M., Swingedouw, D., Szopa, S., Talandier, C., Terray, P., Viovy, N., and Vuichard, N., 2013. Climate change projections using the IPSL–CM5 Earth System Model: from CMIP3 to CMIP5. *Climate Dynamics*, 40(9–10): 2123–2165.

Feng, S., and Fu, Q., 2013. Expansion of global drylands under a warming climate. *Atmospheric Chemistry and Physics*, 13(19): 10081–10094.

Feng, Z.D., Sun, A.Z., Abdusalih, N., Ran, M., Kurban, A., Lan, B., Zhang, D.L., and Yang, Y.P., 2017. Vegetation changes and associated climatic changes in the southern Altai Mountains within China during the Holocene. *The Holocene*, 27(5): 683–693.

Ferronskii, V.I., Polyakov, V.A., Brezgunov, V.S., Vlasova, L.S., Karpychev, Y.A., Bobkov, A.F., Romaniovskii, V.V., Johnson, T., Ricketts, D., and Rasmussen, K., 2003. Variations in the hydrological regime of Kara-Bogaz-Gol Gulf, Lake Issyk-Kul, and the Aral Sea assessed based on data of bottom sediment studies. *Water Resources*, 30(3): 252–259.

Fisher, J.B., Whittaker, R.J., and Malhi, Y., 2011. ET come home: Potential evapotranspiration in geographical ecology. *Global Ecology and Biogeography*, 20(1): 1–18.

Folland, C.K., Rayner, N.A., Brown, S.J., Smith, T.M., Shen, S.S.P., Parker, D.E., Macadam, I., Jones, P.D., Jones, R.N., Nicholls, N., and Sexton, D.M.H., 2001. Global temperature change and its uncertainties since 1861. *Geophysical Research Letters*, 28(13): 2621–2624.

Fu, Q., and Feng, S., 2014. Responses of terrestrial aridity to global warming. *Journal of Geophysical Research: Atmospheres*, 119(13): 7863–7875.

Gent, P.R., Danabasoglu, G., Donner, L.J., Holland, M.M., Hunke, E.C., Jayne, S.R., Lawrence, D.M., Neale, R.B., Rasch, P.J., Vertenstein, M., Worley, P.H., Yang, Z.L., and Zhang, M.H., 2011. The Community Climate System Model Version 4. *Journal of Climate*, 24(19): 4973–4991.

Giorgetta, M.A., Jungclaus, J., Reick, C.H., Legutke, S., Bader, J., Böttinger, M., Brovkin, V., Crueger, T., Esch, M., Fieg, K., Glushak, K., Gayler, V., Haak, H., Hollweg, H.-D., Ilyina, T., Kinne, S., Kornblueh, L., Matei, D., Mauritsen, T., Mikolajewicz, U., Mueller, W., Notz, D., Pithan, F., Raddatz, T., Rast, S., Redler, R., Roeckner, E., Schmidt, H., Schnur, R., Segschneider, J., Six, K.D., Stockhause, M., Timmreck, C., Wegner, J., Widmann, H.,

Wieners, K.-H., Claussen, M., Marotzke, J., and Stevens, B., 2013. Climate and carbon cycle changes from 1850 to 2100 in MPI-ESM simulations for the Coupled Model Intercomparison Project phase 5. *Journal of Advances in Modeling Earth Systems*, 5(3): 572–597.

Gleckler, P.J., Taylor, K.E., and Doutriaux, C., 2008. Performance metrics for climate models. *Journal of Geophysical Research: Atmospheres*, 113(D6): D06104.

Guan, X.F., Yang, L.M., Zhang, Y.X., and Li, J.G., 2019. Spatial distribution, temporal variation, and transport characteristics of atmospheric water vapor over Central Asia and the arid region of China. *Global and Planetary Change*, 172(2019): 159–178.

Hargreaves, G.H., and Samani, Z.A., 1985. Reference crop evapotranspiration from temperature. *Applied Engineering in Agriculture*, 1(2): 96–99.

Held, I.M., and Soden, B.J., 2006. Robust responses of the hydrological cycle to global warming. *Journal of Climate*, 19(21): 5686–5699.

Herzschuh, U., 2006. Palaeo–moisture evolution in monsoonal Central Asia during the last 50,000 years. *Quaternary Science Reviews*, 25(1–2): 163–178.

Holden, P.B., Edwards, N.R., Oliver, K.I.C., Lenton, T.M., and Wilkinson, R.D., 2010. A probabilistic calibration of climate sensitivity and terrestrial carbon change in GENIE-1. *Climate Dynamics*, 35(5): 785–806.

Hong, B., Gasse, F., Uchida, M., Hong, Y.T., Leng, X.T., Shibata, Y., An, N., Zhu, Y.X., and Wang, Y., 2014. Increasing summer rainfall in arid eastern-Central Asia over the past 8500 years. *Scientific Reports*, 4(1): 5279.

Huang, C.Q., 2011. Environmental evolution revealed by pollen records in the central Asia arid zone since the last glacial period (Ph.D. thesis). Lanzhou: Lanzhou University, 1–125.

Huang, W., Chen, F.H., Feng, S., Chen, J.H., and Zhang, X.J., 2013. Interannual precipitation variations in the mid–latitude Asia and their association with large–scale atmospheric circulation. *Chinese Science Bulletin*, 58(32): 3962–3968.

Huang, W., Chen, J.H., Zhang, X.J., Feng, S., and Chen, F.H., 2015. Definition of the core zone of the "westerlies–dominated climatic regime", and its controlling factors during the instrumental period. *Science China Earth Sciences*, 58(5): 676–684.

Huang, X.Z., Chen, F.H., Fan, Y.X., and Yang, M.L., 2009. Dry late-glacial and early Holocene climate in arid central Asia indicated by lithological and palynological evidence from Bosten Lake, China. *Quaternary International*, 194(1–2): 19–27.

Huang, X.Z., Peng, W., Rudaya, N., Grimm, E.C., Chen, X.M., Cao, X.Y., Zhang, J., Pan, X.D., Liu, S.S., Chen, C.Z., and Chen, F.H., 2018. Holocene vegetation and climate dynamics in the Altai Mountains and surrounding areas. *Geophysical Research Letters*, 45(13): 6628–6636.

Jiang, D.B., Su, M.F., Wei, R.Q., and Liu, B., 2009. Variation and projection of drought and wet conditions in Xinjiang. *Chinese Journal of Atmospheric Sciences*, 33(1): 90–98 (in Chinese with English abstract).

Jiang, D.B., and Lang, X.M., 2010. Last Glacial Maximum East Asian monsoon: Results of PMIP simulations. *Journal of Climate*, 23(18): 5030–5038.

Jiang, D.B., Lang, X.M., Tian, Z.P., and Guo, D.L., 2011. Last glacial maximum climate over China from PMIP simulations. *Palaeogeography, Palaeoclimatology, Palaeoecology*, 309(3–4): 347–357.

Jiang, D.B., Lang, X.M., Tian, Z.P., and Wang, T., 2012. Considerable model−data mismatch in temperature over China during the mid-Holocene: Results of PMIP simulations. *Journal of Climate*, 25: 4135–4153.

Jiang, D.B., Lang, X.M., Tian, Z.P., and Ju, L.X., 2013a. Mid-Holocene East Asian summer monsoon strengthening: Insights from Paleoclimate Modeling Intercomparison Project (PMIP) simulations. *Palaeogeography, Palaeoclimatology, Palaeoecology*, 369: 422–429.

Jiang, D.B., Tian, Z.P., and Lang, X.M., 2013b. Mid-Holocene net precipitation changes over China: Model–data comparison. *Quaternary Science Reviews*, 82: 104–120.

Jiang, D.B., Tian, Z.P., and Lang, X.M., 2015a. Mid-Holocene global monsoon area and precipitation from PMIP simulations. *Climate Dynamics*, 44: 2493–2512.

Jiang, D.B., Tian, Z.P., Lang, X.M., Kageyama, M., and Ramstein, G., 2015b. The concept of global monsoon applied to the last glacial maximum: A multi–model analysis. *Quaternary Science Reviews*, 126(2015): 126–139.

Jiang, Q.F., Ji, J.F., Shen, J., Matsumoto, R., Tong, G.B., Qian, P., Ren, X.M., and Yan, D.Z., 2013. Holocene vegetational and climatic variation in westerly-dominated areas of Central Asia inferred from the Sayram Lake in northern Xinjiang, China. *Science China Earth Sciences*, 56(3): 339–353.

Joussaume, S., and Taylor, K.E., 1995. Status of the Paleoclimate Modeling Intercomparison Project (PMIP). In: Gates W L (eds.). Proceedings of the First International AMIP Scientific Conference. World Meteorological Organization: Geneva, 425–430.

Krivonogov, S.K., Kuzmin, Y.V., Burr, G.S., Gusskov, S.A., Khazin, L.B., Zhakov, E.Y., Nurgizarinov, A.N., Kurmanbaev, R.K., and Kenshinbay, T.I., 2010. Environmental changes of the Aral Sea (Central Asia) in the Holocene: Major trends. *Radiocarbon*, 52(2): 555–568.

Leroy, S.A.G., López-Merino, L., Tudryn, A., Chalié, F., and Gasse, F., 2014. Late Pleistocene and Holocene palaeoenvironments in and around the middle Caspian basin as reconstructed from a deep-sea core. *Quaternary Science Reviews*, 101: 91–110.

Li, C.X., and Song, Y.G., 2014. The characteristics of distribution of trace elements and their paleoclimatic implications at the Zhaosu Loess Section in Westerly Area since the Last Glacial Period. *Journal of Earth Environment*, 5(2): 56–66 (in Chinese with English abstract).

Li, L.J., Lin, P.F., Yu, Y.Q., Wang, B., Zhou, T.J., Liu, L., Liu, J.P., Bao, Q., Xu, S.M., Huang, W.Y., Xia, K., Pu, Y., Dong, L., Shen, S., Liu, Y.M., Hu, N., Liu, M.M., Sun, W.Q., Shi, X.J., Zheng, W.P., Wu, B., Song, M.R., Liu, H.L., Zhang, X.H., Wu, G.X., Xue, W., Huang, X.M., Yang, G.W., Song, Z.Y., and Qiao, F.L., 2013. The flexible global ocean–atmosphere–land system model, Grid–point Version 2: FGOALS–g2. *Advances in Atmospheric Sciences*, 30(3): 543–560.

Li, Y., and Morrill, C., 2013. Lake levels in Asia at the Last Glacial Maximum as indicators of hydrologic sensitivity to greenhouse gas concentrations. *Quaternary Science Reviews*, 60(2013): 1–12.

Liu, C.L., Zhang, J.F., Jiao, P.C., and Mischke, S., 2016. The Holocene history of Lop Nur and its palaeoclimate implications. *Quaternary Science Reviews*, 148: 163–175.

Liu, S.S., Jiang, D.B., and Lang, X.M., 2018. A multi–model analysis of moisture changes during the last glacial maximum. *Quaternary Science Reviews*, 191(2018): 363–377.

Liu, X.K., Rao, Z.G., Shen, C.C., Liu, J.B., Chen, J.H., Chen, S.Q., Wang, X.F., and Chen, F.H., 2019. Holocene solar activity imprint on centennial- to multidecadal-scale hydroclimatic oscillations in arid central Asia. *Journal of Geophysical Research: Atmospheres*, 124(5): 2562–2573.
Liu, X.K., Liu, J.B., Shen, C.C., Yang, Y., Chen, J.H., Chen, S.Q., Wang, X.F., Wu, C.C., and Chen, F.H., 2020. Inconsistency between records of δ18O and trace element ratios from stalagmites: Evidence for increasing mid–late Holocene moisture in arid central Asia. *The Holocene*, 30(3): 369–379.
Liu, X.Q., Herzschuh, U., Shen, J., Jiang, Q.F., and Xiao, X.Y., 2008. Holocene environmental and climatic changes inferred from Wulungu Lake in northern Xinjiang, China. *Quaternary Research*, 70(3): 412–425.
Long, H., Shen, J., Chen, J.H., Tsukamoto, S., Yang, L.H., Cheng, H.Y., and Frechen, M., 2017. Holocene moisture variations over the arid central Asia revealed by a comprehensive sand-dune record from the central Tian Shan, NW China. *Quaternary Science Reviews*, 174: 13–32.
Marcott, S.A., Shakun, J.D., Clark, P.U., and Mix, A.C., 2013. A reconstruction of regional and global temperature for the past 11,300 years. *Science*, 339(6124): 1198–1201.
MARGO Project Members, 2009. Constraints on the magnitude and patterns of ocean cooling at the Last Glacial Maximum. *Nature Geoscience*, 2(2): 127–132.
Middleton, N.J., and Thomas, D.S., 1997. World Atlas of Desertification (2nd ed.). London: Arnold.
Mitchell, T.D., and Jones, P.D., 2005. An improved method of constructing a database of monthly climate observations and associated high–resolution grids. *International Journal of Climatology*, 25(6): 693–712.
Monteith, J.L., 1965. Evaporation and environment. *Symposia of the Society for Experimental Biology*, 19: 205–234.
Ohgaito, R., and Abe-Ouchi, A., 2009. The effect of sea surface temperature bias in the PMIP2 AOGCMs on mid-Holocene Asian monsoon enhancement. *Climate Dynamics*, 33(7–8): 975–983.
Overeem, I., Kroonenberg, S.B., Veldkamp, A., Groenesteijn, K., Rusakov, G.V., and Svitoch, A.A., 2003. Small–scale stratigraphy in a large ramp delta: Recent and Holocene sedimentation in the Volga delta, Caspian Sea. *Sedimentary Geology*, 159(3–4): 133–157.
Penman, H.L., and Keen, B.A., 1948. Natural evaporation from open water, bare soil and grass. *Proceedings of the Royal Society of London. Series A. Mathematical and Physical Sciences*, 193(1032): 120–145.
Quade, J., and Broecker, W.S., 2009. Dryland hydrology in a warmer world: Lessons from the Last Glacial period. *The European Physical Journal Special Topics*, 176(1): 21–36.
Rasmussen, K.A., Ricketts, R.D., Johnson, T.C., Romanovsky, V.V., and Grigina, O.M., 2001. An 8,000 year multi-proxy record from Lake Issyk-Kul, Kyrgyzstan. *PAGES* (Past Global Changes) *News*, 9 (2): 5–6.
Ricketts, R.D., Johnson, T.C., Brown, E.T., Rasmussen, K.A., and Romanovsky, V.V., 2001. The Holocene paleolimnology of Lake Issyk-Kul, Kyrgyzstan: Trace element and stable isotope composition of ostracodes. *Palaeogeography, Palaeoclimatology, Palaeoecology*, 176(1–4): 207–227.
Shi, Y.F., Shen, Y.P., Kang, E., Li, D.L., Ding, Y.J., Zhang, G.W., and Hu, R.J., 2007. Recent and future climate change in Northwest China. *Climatic Change*, 80(3–4): 379–393.
Shindell, D.T., Pechony, O., Faluvegi, G.S., Voulgarakis, A., Nazarenko, L.S., Lamarque, J.-F., Bowman, K., Milly, G.P., Kovari, W., Ruedy, R., and Schmidt, A.G., 2013. Interactive ozone and methane chemistry in GISS–E2 historical and future climate simulations. *Atmospheric Chemistry Physics*, 13(5): 2653–2689.
Sun, A.Z., Feng, Z.D., Ran, M., and Zhang, C.J., 2013. Pollen-recorded bioclimatic variations of the last ~22,600 years retrieved from Achit Nuur core in the western Mongolian Plateau. *Quaternary International*, 311: 36–43.
Tao, S.C., An, C.B., Chen, F.H., Tang, L.Y., Wang, Z.L., Lü, Y.B., Li, Z.F., Zheng, T.M., and Zhao, J.J., 2010. Pollen-inferred vegetation and environmental changes since 16.7 ka BP at Balikun Lake, Xinjiang. *Chinese Science Bulletin*, 55(22): 2449–2457.
Tian, F., Herzschuh, U., Telford, R.J., Mischke, S., Van der Meeren, T., and Krengel, M., 2014. A modern pollen–climate calibration set from central-western Mongolia and its application to a late glacial–Holocene record. *Journal of Biogeography*, 41(10): 1909–1922.
Tian, Z.P., and Jiang, D.B., 2013. Mid-Holocene ocean and vegetation feedbacks over East Asia. *Climate of the Past*, 9: 2153–2171.
Tian, Z.P., and Jiang, D.B., 2015. Mid-Holocene ocean feedback on global monsoon area and precipitation. *Atmospheric and Oceanic Science Letters*, 8: 29–32.
Tian, Z.P., and Jiang, D.B., 2016. Revisiting last glacial maximum climate over China and East Asian monsoon using PMIP3 simulations. *Palaeogeography, Palaeoclimatology, Palaeoecology*, 453: 115–126.
Tian, Z.P., and Jiang, D.B., 2018. Strengthening of the East Asian winter monsoon during the mid-Holocene. *The Holocene*, 28(9): 1443–1451.
Voldoire, A., Sanchez-Gomez, E., Salas y Mélia, D., Decharme, B., Cassou, C., Sénési, S., Valcke, S., Beau, I., Alias, A., Chevallier, M., Déqué, M., Deshayes, J., Douville, H., Fernandez, E., Madec, G., Maisonnave, E., Moine, M.-P., Planton, S., Saint-Martin, D., Szopa, S., Tyteca, S., Alkama, R., Belamari, S., Braun, A., Coquart, L., and Chauvin, F., 2013. The CNRM–CM5.1 global climate model: Description and basic evaluation. *Climate Dynamics*, 40(9–10): 2091–2121.
Wang, N., Jiang, D.B., and Lang, X.M., 2018. Northern westerlies during the Last Glacial Maximum: Results from CMIP5 simulations. *Journal of Climate*, 31(3): 1135–1153.
Wang, Q., Wei, H.T., Khormali, F., Wang, L.B., Xie, H.C., Wang, X., Huang, W., Chen, J.H., and Chen, F.H., 2020. Holocene moisture variations in western arid central Asia inferred from loess records from NE Iran. *Geochemistry, Geophysics, Geosystems*, 21(3): e2019GC008616.
Wang, T., Wang, H.J., and Jiang, D.B., 2010. Mid-Holocene East Asian summer climate as simulated by the PMIP2 models. *Palaeogeography, Palaeoclimatology, Palaeoecology*, 288(1–4): 93–102.
Wang, T., Liu, Y., and Huang, W., 2013. Last Glacial Maximum sea surface temperatures: A model-data comparison. *Atmospheric and Oceanic Science Letters*, 6(5): 233–239.
Wang, T., and Wang, H.J., 2013. Mid-Holocene Asian summer climate and its responses to cold ocean surface simulated in the PMIP2 OAGCMs experiments. *Journal of Geophysical Research: Atmospheres*, 118(10): 4117–4128.
Wang, W., Feng, Z.D., Ran, M., and Zhang, C.J., 2013. Holocene climate and vegetation changes inferred from pollen records of Lake Aibi, northern Xinjiang, China: A potential contribution to understanding of Holocene climate pattern in East-central Asia. *Quaternary International*, 311: 54–62.
Wang, W., and Zhang, D.L., 2019. Holocene vegetation evolution and climatic dynamics inferred from an

ombrotrophic peat sequence in the southern Altai Mountains within China. *Global and Planetary Change*, 179: 10–22.
Wang, Y.J., Zhou, B.T., Qin, D.H., Wu, J., Gao, R., and Song, L.C., 2017. Changes in mean and extreme temperature and precipitation over the arid region of northwestern China: Observation and projection. *Advances in Atmospheric Sciences*, 34(3): 289–305.
Watanabe, S., Hajima, T., Sudo, K., Nagashima, T., Takemura, T., Okajima, H., Nozawa, T., Kawase, H., Abe, M., Yokohata, T., Ise, T., Sato, H., Kato, E., Takata, K., Emori, S., and Kawamiya, M., 2011. MIROC–ESM 2010: Model description and basic results of CMIP5–20c3m experiments. *Geoscientific Model Development*, 4(4): 845–872.
Wünnemann, B., Mischke, S., and Chen, F.H., 2006. A Holocene sedimentary record from Bosten Lake, China. *Palaeogeography, Palaeoclimatology, Palaeoecology*, 234(2–4): 223–238 (in Chinese with English abstract).
Yang, L.M., and Zhu, B.Q., 2018. Environmental changes and landform evolution of the Alashan Plateau region during the Last Glacial period since 40 ka. *Acta Geologica Sinica*, 92(12): 2561-2581.
Yang, L.M., Guan, X.F., and Zhang, Y.X., 2018. Atmospheric circulation characteristics of precipitation anonaly in arid regions in Central Asia. *Arid Zone Research*, 35(2): 249–259 (in Chinese with English abstract).
Yang, X.X., Kong, Z.C., Jiang, W.Y., and Yang, S.L., 2012. Pollen record for the Weiyuan loess section since the Last Glacial Maximum. *Journal of Earth Environment*, 3(2): 819–825 (in Chinese with English abstract).
Yu, G., Chen, X., Ni, J., Cheddadi, R., Guiot, J., Han, H., Harrison, S.P., Huang, C., Ke, M., Kong, Z., Li, S., Li, W., Liew, P., Liu, G., Liu, J., Liu, Q., Liu, K.-B., Prentice, I.C., Qui, W., Ren, G., Song, C., Sugita, S., Sun, X., Tang, L., Van Campo, E., Xia, Y., Xu, Q., Yan, S., Yang, X., Zhao, J., and Zheng, Z., 2000. Palaeovegetation of China: A pollen data–based synthesis for the mid–Holocene and Last Glacial Maximum. *Journal of Biogeography*, 27(3): 635–664.
Yukimoto, S., Adachi, Y., Hosaka, M., Sakami, T., Yoshimura, H., Hirabara, M., Tanaka, T.Y., Shindo, E., Tsujino, H., Deushi, M., Mizuta, R., Yabu, S., Obata, A., Nakano, H., Koshiro, T., Ose, T., and Kitoh, A., 2012. A new global climate model of the Meteorological Research Institute: MRI–CGCM3 — Model description and basic performance&mdash. *Journal of the Meteorological Society of Japan*, 90A: 23–64.
Zhang, C.J., Dembele, B., Zhang, W.Y., Zhang, J.Y., Wang, H.S., E, G., and Zheng, Q., 2018b. The Low Lake-Level Record according to the Selin Co Stratigraphical Basis and Multi-Proxies during the Last Glacial Maximum in the Central Tibetan Plateau. *Acta Geologica Sinica (English Edition)*, 92(5): 2058-2059.
Zhang, H.R., DeMbele, B., Zhang W.Y., Zhang, J.Y., Ma, Y., and Zhang, C.J., 2018a. The Dry-Cold Climate of the Qijia Archeological Civilization in Chankou of the Loess Plateau along the Silk Road Since the Neolithic Period. *Acta Geologica Sinica (English Edition)*, 92(6): 2466-2467.
Zhang, Y., Meyers, P.A., Liu, X.T., Wang, G.P., Ma, X.H., Li, X.Y., Yuan, Y.X., and Wen, B.L., 2016. Holocene climate changes in the central Asia mountain region inferred from a peat sequence from the Altai Mountains, Xinjiang, northwestern China. *Quaternary Science Reviews*, 152: 19–30.
Zhang, Y., Yang, P., Tong, C., Liu, X.T., Zhang, Z.Q., Wang, G.P., and Meyers, P.A., 2018. Palynological record of Holocene vegetation and climate changes in a high-resolution peat profile from the Xinjiang Altai Mountains, northwestern China. *Quaternary Science Reviews*, 201: 111–123.
Zhao, Y., Braconnot, P., Harrison, S.P., Yiou, P., and Marti, O., 2007. Simulated changes in the relationship between tropical ocean temperatures and the western African monsoon during the mid-Holocene. *Climate Dynamics*, 28(5): 533–551.
Zhou, B.T., and Zhao, P., 2009. Inverse correlation between ancient winter and summer monsoons in East Asia? *Chinese Science Bulletin*, 54(20): 3760–3767.
Zhou, B.T., and Zhao, P., 2010. Modeling variations of summer upper tropospheric temperature and associated climate over the Asian Pacific region during the mid-Holocene. *Journal of Geophysical Research: Atmospheres*, 115(D20): D20109.
Zhou, B.T., and Zhao, P., 2013. Simulating changes of spring Asian-Pacific oscillation and associated atmospheric circulation in the mid-Holocene. *International Journal of Climatology*, 33: 529–538.

About the first author
XU Hongna, female, born in 1994. Now, she is a Master degree candidate in school of atmospheric sciences, Nanjing University of Information Science & Technology. E-mail: Hongnaxu@163.com.

About the corresponding author
WANG Tao, male, professor, currently works at the Institute of Atmospheric Physics, Chinese Academy of Sciences. He does research in Climatology and paleoclimate modelling. E-mail: wangtao@mail.iap.ac.cn.

Fig. 1. Map shows the core zone of arid Central Asia, including Central Asia (35°–50°N, 50°–75°E, the left rectangle) and Xinjiang area in China (40°–50°N, 75°–95°E, the right rectangle).

Fig. 2. Observed SAT (unit: °C) for (a) annual mean, (b) spring, (c) summer, (d) autumn, and (e) winter based on CRU data in the period of 1901–2000; The MMM of simulated SAT (unit: °C) for (f) annual mean, (g) spring, (h) summer, (i) autumn, and (j) winter based on the PMIP3 PI simulations; And (k–o) the corresponding differences in SAT between the MMM and observation. Dots in (k–o) denote that at least 5 out of 8 models agree on the sign of MMM's biases.

Fig. 3. Observed precipitation (unit: mm/d) for (a) annual mean, (b) spring, (c) summer, (d) autumn, and (e) winter based on CRU data in the period of 1901–2000; The MMM of simulated precipitation (unit: mm/d) for (f) annual mean, (g) spring, (h) summer, (i) autumn, and (j) winter based on the PMIP3 PI simulations; And (k–o) the corresponding differences in precipitation between the MMM and observation. Dots in (k–o) denote that at least 5 out of 8 models agree on the sign of the MMM's biases.

Fig. 4. The observed and MMM of simulated annual cycle of SAT (unit: °C) over the (a) Central Asia (35–50°N, 50–75°E) and (b) Xinjiang (40–50°N, 75–95°E) based on the CRU data and PMIP3 PI simulations. (c-d) Same as (a–b) but for the precipitation (unit: mm/d).

Fig. 5. (a–e) The MMM of simulated annual and seasonal mean SAT (unit: °C) based on the PMIP3 PI simulations. The MMM of simulated changes in annual and seasonal mean SAT (unit: °C) for the (f–j) MH and (k–o) LGM simulations with relative to the PI simulation. Dots in (f–o) denote that at least 5 out of 8 models agree on the sign of the MMM.

Fig. 6. (a–e) The MMM of simulated annual and seasonal mean precipitation (unit: mm/d) based on the PMIP3 PI simulations. The MMM of simulated changes in annual and seasonal mean precipitation (unit: mm/d) for the (f–j) MH and (k–o) LGM simulations with relative to the PI simulation. Dots in (f–o) denote that at least 5 out of 8 models agree on the sign of the MMM.

Fig. 7. The MMM of simulated changes in annual cycle of SAT (unit: °C) over the (a) Central Asia (35–50°N, 50–75°E) and (b) Xinjiang (40–50°N, 75–95°E) for the MH (orange line) and LGM (blue line) relative to that in the PI (gray line). (c-d) Same as (a–b) but for the precipitation (unit: mm/d).

Fig. 8. (a–b) The MMM of simulated AI in the PI. The MMM of simulated changes of AI (%) for the (c–d) MH and (e–f) LGM relative to AI in the PI. Black dots denote that at least 3 out of 5 (5 out of 8) models agree on the sign of the MMM using the PM (HG) method. (a), (c), and (e) are calculated by the PM method. (b), (d), and (f) are calculated by the HG method.

Fig. 9. The AI changes (%, relative to PI) caused by changes in (a–b) precipitation and (c–d) PET using the PM and HG methods for the MH period. (e–h) Same as (a-d), but for the LGM. Black dots denote that at least 3 out of 5 (5 out of 8) models agree on the sign of the MMM using the PM (HG) method.

Fig. 10. The AI changes (%, relative to PI) caused by (a) Tmean, (b) RH, (c) AE, and (d) U using the PM methods for the MH period. (e–h) Same as the (a-d), but for the LGM. Black dots denote that at least 3 out of 5 models agree on the sign of the MMM.

Fig. 11. Reconstructed moisture changes for the (a) MH and (b) LGM. The backgrounds of them are the changes of AI using the PM method, which are same as Fig. 8c and 8e, respectively.